Tampere University

Lucero Cárdenas Razo

DESIGN OF ALL-FIBER, SINGLE CAVITY DUAL-COMB LASER

Master of Science Thesis
Faculty of Engineering and Natural Sciences
Examiners: Dr. Regina Gumenyuk
and Dr. Mikko Närhi
October 2022

ABSTRACT

Lucero Cárdenas Razo: Design of all-fiber, single cavity dual-comb laser
Master of Science Thesis
Tampere University
October 2022

Dual-comb spectroscopy (DCS) has proven to be a powerful technique for high-resolution and high sensitivity broadband spectroscopy, but the cost and complexity of the available laser sources has limited its application beyond research laboratories. A recent approach, aiming to simplify the DCS laser sources, reduce their cost and extend this spectroscopy technique for industrial applications, has been to develop dual-comb fiber lasers that emit two combs from a single cavity. In this thesis, an experimental and numerical study of a novel design of a bidirectional dual-comb fiber laser based in an all-normal, all-polarization maintaining (PM) fiber scheme is proposed. The experimental demonstration of this laser was limited to independent mode-locked operation in both directions, but the simultaneous dual-comb operation was not successful. A numerical study gave insights into the problem investigation and identified the key parameters preventing the dual-comb operation. The method followed to simulate the dual-comb was to replicate the experimental cavity by modeling independently each component of the oscillator and transmitting a pulse through for a fixed number of roundtrips. The simulations showed that the insertion losses of the cavity components were determinant to obtain dual-comb solutions. Additionally, it was shown that this dependence was characteristic of the dual-comb design, and not observed in single comb cavities with similar properties. Simulations also suggest that the reason why the experimental dual-comb was not achieved was possibly due to the imbalance of the losses and coupled gain inside the cavity. Another possible reason is that in the experiments, different SESAMs were used in both directions. These results provide insights about some determinant cavity parameters for dual-comb operation, helping to improve the design to successfully achieve dual-comb operation.

Keywords: fiber lasers, dual frequency comb, mode-locked lasers, ytterbium lasers

PREFACE

The purpose of this text is to present the results of the research conducted in the Advanced Coherent Sources Group of the Photonics Department in Tampere University. With this thesis report, I complete the Europhotonics Joint Master's studies in both Aix-Marseille Université and Tampere University.

First, I want to express my gratitude to Dr. Regina Gumenyuk for granting me the opportunity to work in her group. Thank you for support, trust and for the constant feedback. I also want to thank Dr. Mikko Närhi for guiding me through all the stages of this project, providing laboratory training and numerical simulations code. Thank you for your suggestions, time, and patience to answer all my questions. I also want to thank my group mates, Iuliia, Hossein and Leo for the help provided during my experiments and for the nice atmosphere in the laboratory. A special mention to Dr. Eero Koivusalo, who kindly provided the SESAM samples used in this study and a nice discussion about these devices. Aknowledgements to the Computational Science Center of Finland, for the supercomputer resources provided to perform the numerical simulations in this work.

Additional thanks to my collegues in the ORC who made my thesis experience not only about lab work and simulations, but also about enjoying the long nordic summer nights, food adventure trips and the Finnish woods: Abhiroop, Phillip, Lea, David and Jaime.

Extra aknowlegments to my (virtual) friends from Europhotonics with whom I shared parts of my master studies these two years: The mexican *gang* (Lucerito, Nayla, Steph, Sergio), my *pieni* Tampere family (Sarah and Oriol) and the musicians (Enric and Ravi). And to Narmin and Vlad, because they are mexican by transitivity. Marsella da, Marsella quita, *that's what she said.* Also thanks to my dear friends in Mexico with whom I am tangled in a spooky action at a distance: Diana, Iván, Abraham and Siddhartha, for the laughs, company and support during all these years.

At last, I want to dearly thank my parents and my brother for always motivating me to achieve my goals and aspirations, even when they take me very far from them. Your love is always crossing oceans. Home is where you are.

In memory of mama Licha, Francisco and Estefanía.

Tampere, 23rd October 2022

Lucero Cárdenas Razo

CONTENTS

LIST OF SYMBOLS AND ABBREVIATIONS

A_{eff}	Effective area
$A(z,T)$	Complex amplitude of the electric field
ANDi	All-normal dispersion
ASE	Amplified spontaneous emission
α	Attenuation parameter
BPF	Bandpass filter
BW	Bandwidth
β_2	Group velocity dispersion parameter (GVD)
β_1	Group delay
$\boldsymbol{B}$	Magnetic flux density
$\beta(\omega)$	Propagation constant
CCW	Anti-clockwise direction
CW	Clockwise direction
CIRC	Circulator
c	Speed of light in vaccuum
ΔR_{ns}	Non-saturable loss
ΔR	Modulation depth
D	Dispersion parameter
$\boldsymbol{D}$	Electric displacement
Er	Erbium
ε_0	Vacuum permitivity
FDTDM	Finite diference time domain method
F_{sat}	Saturation fluence
f_R	Repetition rate
FWHM	Full-width at half-maximum
GCO	Gigant chirp oscillators
GNLSE	Generalized nonlinear Schrödinger equation

γ	Nonlinear parameter
Ho	Holmium
$\boldsymbol{H}$	Magnetic field
IL	Insertion losses
$\boldsymbol{J}$	Free current density
KLM	Kerr-Lens Mode-locking
L_{NL}	Nonlinear length
L_D	Dispersive length
MBD	Molecular beam epitaxy
MIXSEL	Mode-locked integrated external-cavity surface emitting laser
ML	Mode-locking
μ_0	Vacuum permeability
$\boldsymbol{M}$	Magnetization
NALM	Nonlinear amplifying loop mirrors
n_{eff}	Effective refractive index
n_2	Kerr coefficient
NLSE	Nonlinear Schrödinger equation
NPR	Nonlinear polarization rotation
NA	Numerical aperture
OFC	Optical frequency comb
OC	Output coupler
PCF	Photonic crystal fiber
PM	Polarization maintaining fiber
P_{sat}	Saturation power
ρ	Free charge density
$\boldsymbol{P}$	Polarization
R_{lin}	Linear reflectivity
R_{ns}	Maximum reflectivity
SESAM	Semiconductor Saturable Absorber Mirror
SSB	Stimulated Brillouin scattering
SI	International system of units
SMF	Single mode fiber

SPM	Self-phase modulation
SRS	Stimulated Raman scattering
SSF	Split-step Fourier method
SWNTs	Single wall carbon nanotubes
τ_{rec}	Recovery time
THG	Third harmonic generation
T_R	Roundtrip time of the pulse inside the cavity
Tm	Thulium
T_0	Pulse duration
Tm	Thulium
V	V-value or normalized frequency
v_g	Group velocity
WDM	Wavelength division multiplexer
χ_m	Magnetic susceptibility
χ_e	Electric susceptibility
Yb	Ytterbium

1. INTRODUCTION

An optical frequency comb is a spectrum formed by narrow, evenly-spaced optical frequencies that share a common phase evolution [1, 2]. This type of spectra is observed in sources that emit pulse trains, as mode-locked lasers. The first laser of this type utilized Nd:glass as gain medium and a dye as a saturable absorber [3]. It was developed soon after the first laser was demonstrated and it represented the starting point for the development of ultrashort pulse sources. During the 90's, the advent of femtosecond laser systems established on new passive mode-locking techniques, mainly saturable absorbers based on semiconductors or Kerr lens mode-locking, provided a new approach to produce stable pulse trains [4]. These lasers soon provided a versatile operation with ultrashort pulses, high peak intensity and repetition rate, and broad spectral bandwidth [4]. These characteristics made them attractive and quickly found application in astronomical spectrograph calibration, optical communications, distance measurements and laser ranging, and attosecond generation [2, 4, 5]. Another point to remark on is the positive feedback loop habitually shared between laser development and their applications. An example of relevant attention is found in the optical frequency metrology field, where optical frequency combs were first introduced to use them as a reference to measure the cycles from optical atomic clocks [2]. As a result of their research performed in this field and their contributions to developing frequency combs, Theodor Hänsch and John Hall were awarded the Nobel Prize in Physics in 2005 [2].

Frequency comb spectroscopy is recognized as the first application of a frequency comb [1]. Relying on the aforementioned characteristics of these sources, primarily broad spectral bandwidth, spatial coherence and high-frequency resolution, different spectral regions and multiple spectroscopy techniques have been developed. Examples include direct frequency comb spectroscopy, Michelson-based Fourier transform spectroscopy and dual-comb spectroscopy [1, 6]. The latter scheme has been widely investigated, mainly because its implementation is free of moving parts, leading to a simplification of the optical setup. The principle of this technique is that one of the combs analyzes the sample, acquiring the spectral information in its amplitude and phase. Then both combs interfere with each other, leading to an optical interferogram in time domain. In the frequency domain, it corresponds to a spectrum in the radio-frequencies (RF) that can be recorded with digital RF analyzers [1]. Due to the interferometric nature of the technique, mutual coher-

ence between the two combs is required. One approach to achieve it, is to use advanced frequency stabilization systems to lock the phase of both combs. This direction requires complex and costly infrastructure, limiting the application of dual-comb spectroscopy beyond research laboratories. The second approach to achieve mutual coherence, widely explored in recent years, is to design lasers with a naturally occurring mutual coherence system in the cavity. Bidirectional mode-locked lasers are examples of laser designs that integrate both combs in the same cavity, achieving mutual stabilization without electronic systems. Several designs have been demonstrated, such as a dual-comb based on a single Ti:Sapph ring laser [7], a mode-locked integrated external-cavity surface emitting laser (MIXSEL) [8] and fiber lasers.

Frequency combs based on mode-locked fiber lasers are compact, robust and inexpensive [5]. Due to their simple designs assembled by off-the-shelf components, they have been studied as sources for dual-comb spectroscopy. In fact, fiber lasers developed for this application are available in the market, however the design is not single cavity [9].
In 2008, the first all-fiber bidirectional single cavity, Erbium-doped ring-shaped laser was demonstrated [10]. This laser made use of a saturable absorber based on carbon nanotubes to achieve the mode-locking regime. However, polarization control was required to optimize the output pulses. This laser and other single cavity dual-comb designs introduced free-space components in the cavity to achieve dual-comb operation [5, 11]. Introducing free-space elements limits the application of these sources in industrial environments, where any fluctuations might lead to bad performance of the devices [12].

The first Ytterbium based all-normal, all-PM fiber, single cavity, dual-comb laser is yet to be demonstrated. The research presented in this thesis aims to develop this laser. The features of its design are proposed to improve the cavity stability with aims to a possible application in industry. An all-normal fiber allows a cavity configuration with elements that do not require optical alignment. At the same time, polarization maintaining (PM) fiber is proposed to improve robustness. Moreover, the cost of the dual-comb system is reduced compared to using two single combs, because only a single laser is required and no stabilization methods to lock the phases of both combs are needed. Finally, the interest in using Ytterbium (Yb) lasers is to provide larger pulse energies, compared to Erbium (Er) based lasers [13], as well as applying an all-normal dispersion laser configuration (ANDi).

Project objectives

The objectives of this thesis encompass two directions:

(I) Experimental demonstration of a dual-comb laser novel design

  (1) Build an experimental demonstration of an all-normal, all-PM fiber, Yb-based single cavity dual-comb, passively mode-locked by two semiconductor saturable absorber mirrors (SESAMs). The laser operation is all-normal dispersion regime, generating dissipative solitons.

(II) Numerical simulations

  (1) Numerically study the principal design issues of such lasers. This will be done by simulating independently each cavity component and transmitting a pulse through, to find the adequate parameters of each cavity element to achieve the dual-comb operation.

Thesis Structure

The structure of the thesis consists in 5 chapters. It starts with a brief introduction, that will settle the context for the development of single-cavity, dual-comb lasers. It will be followed by Chapter 2, where a theoretical background on light propagation in optical fibers, including the description of linear and nonlinear effects, is described. This will serve as a foundation to understand the operational properties inside the cavity that determine the dual-comb. Chapter 3 is dedicated to discussing the fundamentals of all-normal dispersion fiber lasers (ANDi). Here, the cavity design proposal will be introduced, describing the cavity components and how they are modeled numerically. In Chapter 4, a discussion about the experimental dual-comb will be presented. The section will also include the results of the numerical simulations performed to understand the balance of gain and losses in the cavity. Finally, Chapter 5 will discuss the conclusions and future outlook of the research project.

2. LIGHT PROPAGATION IN OPTICAL FIBERS

Even when the phenomenon of total internal reflection was known since the first optical experiments were performed in the 19th century, the fabrication of good quality optical fibers was possible only from the 1950s due to pioneering work of C. Kao [14]. During the 1970s, these waveguides were exploited in telecommunications, providing a high quality optical confinent with low attenuation across great distances. Moreover, the development of fibers also contributed to the rise of the nonlinear fiber optics field due to the long interaction lengths provided by this type of waveguides. During the 1990's, the experimental observation of nonlinear phenomena as optical solitons, self-phase modulation, stimulated Raman scattering, and others, compiled enough experimental and theoretical research to establish new ultrashort laser sources.

The fabrication of fibers doped with rare-earth materials such as Erbium (Er), represented again a turning point in telecommunications, especially in the third telecommunication window, at 1.55 μm. They allowed the fabrication of new fiber amplifiers that were used to compensate for the transmission losses, improving the efficiency. At the same time, Ytterbium (Yb) and Thulium (Tm) doped fibers provided a way to ensure laser operation in different spectral regions.

In the early 2000's, new fibers with complex cross sections were demonstrated, such as microstructured fibers and photonic band gap fibers [15]. Combined with their small core size, they enhanced the nonlinear effects even further and led to the rise of a new field of study, supercontinuum generation [16]. The development of new fiber technologies has fueled the progress of many adjacent fields, such as ultrafast optics, laser development, and telecommunications [14]. In recent years, other fields as biophotonics have exploited the potential of fiber optics to develop imaging systems and sensors [17], for example.

In this chapter, a brief introduction will present the main characteristics of optical fibers in the context of our study. Then, the physical and mathematical description of the linear and nonlinear effects in optical fibers that will be important to understand the propagation of pulses in the proposed fiber dual-comb laser will be described.

2.1 Properties of optical fibers

An optical fiber is a cylindrical waveguide. Its structure is formed by a glass core, where light is guided, and a surrounding glass layer, called cladding. Light is confined at the core-cladding boundary by total internal reflection, implying that the refractive index of the core n_{core}, is higher than the one in the cladding, n_{clad}. The refractive index profile of these fibers is called step-index due to the abrupt difference between the values at the core-cladding interface. Other types of fibers called graded-index fibers have a continuous refractive index that decreases radially. An important parameter to describe optical fibers is the V-value (or normalized frequency) of the fiber [18]. It is defined as $V = \frac{2\pi a NA}{\lambda}$, where a is the core radius, NA is the numerical aperture of the fiber and λ is the operative wavelength. For values $V < 2.405$, the fibers can only support the propagation of the fundamental optical mode, so these types of fibers are called single mode (SM). Typical fiber core sizes are 6 μm and 10 μm, typically used for wavelengths 1.05 μm and 1.55 μm, respectively. The most common materials used to fabricate fibers are oxide based glass, with silica (SiO_2). Other oxides can be added to increase the refractive index of the silica, as aluminum oxide (Al_2O_3) or phosphorus oxide (P_2O_5).

2.2 Linear light propagation in optical fibers

I begin the discussion of the pulse propagation in optical fibers following the derivation presented in [14]. First, we consider the four Maxwell's equations expressed in SI units in the time domain:

$$\nabla \cdot \boldsymbol{D} = \rho_f \tag{2.1}$$

$$\nabla \cdot \boldsymbol{B} = 0 \tag{2.2}$$

$$\nabla \times \boldsymbol{E} = -\frac{\partial \boldsymbol{B}}{\partial t} \tag{2.3}$$

$$\nabla \times \boldsymbol{H} = \frac{\partial \boldsymbol{D}}{\partial t} + \boldsymbol{J} \tag{2.4}$$

where $\boldsymbol{D}$ represents the electric displacement, $\boldsymbol{E}$ the electric field, $\boldsymbol{B}$ the magnetic flux density, $\boldsymbol{H}$ the magnetic field, ρ the free charge density and $\boldsymbol{J}$ the free current density. The constitutive relations describe the interaction of these fields in presence of isotropic and homogeneous materials:

$$\boldsymbol{D} = \varepsilon_0 \boldsymbol{E} + \boldsymbol{P} = \varepsilon_0 \boldsymbol{E} + \varepsilon_0 \chi_e \boldsymbol{E} \tag{2.5}$$

$$\boldsymbol{B} = \mu_0 \boldsymbol{H} + \boldsymbol{M} = \mu_0 \boldsymbol{H} + \mu_0 \chi_m \boldsymbol{H} \tag{2.6}$$

where $\boldsymbol{P}$ represents the polarization, $\boldsymbol{M}$ describes the magnetization, χ_e and χ_m denote the electric and magnetic susceptibility and the relation between the speed of light c, the vacuum permitivity ε_0 and the vacuum permeability μ_0, $c^2 = \frac{1}{\varepsilon_0 \mu_0}$ holds. Optical fibers are typically made of dielectric materials, such as glass. Therefore, they do not accumulate free electrons or charges on their surface and do not conduct electrical current. Thus, $\boldsymbol{J} = 0$ and $\rho_f = 0$. Moreover, the glasses are non-magnetic, so the effects related to the magnetic susceptibility χ_m are null. Likewise, the glasses are assumed to be isotropic and homogeneous, so the tensor χ_e is simplified to a scalar quantity [14]. These simplifications lead to the Maxwell's equations for dielectric media:

$$\nabla \cdot \boldsymbol{D} = 0 \tag{2.7}$$

$$\nabla \cdot \boldsymbol{B} = 0 \tag{2.8}$$

$$\nabla \times \boldsymbol{E} = -\frac{\partial \boldsymbol{B}}{\partial t} \tag{2.9}$$

$$\nabla \times \boldsymbol{H} = \frac{\partial \boldsymbol{D}}{\partial t} \tag{2.10}$$

with constitutive relations:

$$\boldsymbol{D} = \varepsilon_0 \boldsymbol{E} + \varepsilon_0 \chi_e \boldsymbol{E} \tag{2.11}$$

$$\boldsymbol{B} = \mu_0 \boldsymbol{H} \tag{2.12}$$

Equations 2.7-2.10 form a set of first order, coupled, partial differential equations for both fields. Combining them, they can be decoupled into two equations, one for each field. We will focus on the example of the electric field. Taking the curl of Eq. 2.9, replacing $\boldsymbol{B}$ as in Eq. 2.12 and then replacing the right side by Eq. 2.10, plus substituting the definition of $\boldsymbol{D}$ and using the vectorial relation on the left side $\nabla \times \nabla \times \boldsymbol{E} = \nabla (\nabla \cdot \boldsymbol{E}) - \nabla^2 \boldsymbol{E}$, it is possible to get the expression:

$$\nabla^2 \boldsymbol{E} = \mu_0 \varepsilon_0 \frac{\partial^2 \boldsymbol{E}}{\partial t^2} - \mu_0 \varepsilon_0 \chi_e \frac{\partial^2 \boldsymbol{E}}{\partial t^2} \tag{2.13}$$

Now, grouping terms and using the relation $c^2 = \frac{1}{\varepsilon_0 \mu_0}$, the previous expression is:

$$\nabla^2 \boldsymbol{E} = \mu_0 \varepsilon_0 (1 + \chi_e) \boldsymbol{E} \tag{2.14}$$

$$= \frac{1}{c^2} \frac{\partial^2 \boldsymbol{E}}{\partial t^2} + \frac{1}{\varepsilon_0 c^2} \frac{\partial^2 \boldsymbol{P}}{\partial t^2} \tag{2.15}$$

Written in this form, we can recognize a non-homogeneous wave equation for the electric field where the source term depends on the polarization of the material. Without this term, the solution for this equation are waves propagating with velocity c/n, where n represents the refractive index of the propagation material.

2.2.1 Linear effects in optical fibers

Examining Eq. 2.14, it is possible to observe that if the polarization $\boldsymbol{P}$ has a linear relation with the electric field $\boldsymbol{E}$ as in Eq. 2.11, then the total response of the system will be purely linear. To illustrate this, in Eq. 2.13 is possible to observe that the propagation of the electric field is determined by the material response, given by the electric susceptibility. This quantity in general is defined as a complex number. The real part of this quantity is connected to the refractive index and the imaginary part is associated with the losses of the material by the following relations:

$$n = Re\left\{\sqrt{1+\chi_e}\right\} \tag{2.16}$$

$$\alpha = \frac{\omega}{nc} Im\left\{\chi_e\right\} \tag{2.17}$$

where ω is the angular frequency of the propagating field. Therefore, linear effects in optical fibers result from variations in the refractive index or in the attenuation of a pulse when it propagates.

Chromatic dispersion

Material dispersion is the frequency dependence of the refractive index of optical materials. This dependence can be explained by considering that the electrons bound to the nucleus will oscillate differently depending on the frequency (energy) of the electromagnetic radiation that irradiates them. Figure 2.1 shows in red a plot that describes the material dispersion for bulk fused silica, commonly expressed in terms of wavelength.

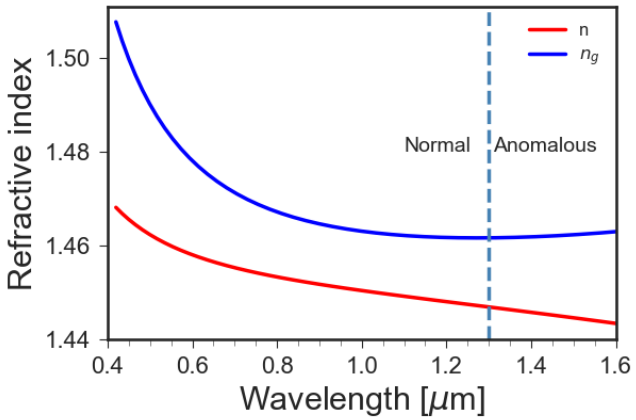

Figure 2.1. *Refractive index dependency on wavelength for bulk fused silica. Data obtained from [19] and adapted from a figure in [14].*

The effect of fiber dispersion is that the different spectral components of a pulse will travel at different velocities given by $c/n(\omega)$, leading to a time delay. To quantify this delay, in

principle it is required to know how fast a spectral component ω propagates.
This is determined by the propagation constant: $\beta(\omega) = \frac{n(\omega)\omega}{c}$. Typically the propagation constant β is expanded around the center frequency of the pulse ω_0 as a Taylor series:

$$\beta(\omega) = n(\omega)\frac{\omega}{c} = \beta_0 + \beta_1(\omega - \omega_0) + \frac{1}{2}\beta_2(\omega - w_0)^2 + \dots \tag{2.18}$$

where $\beta_m = \left(\frac{d^m\beta}{d\omega^m}\right)_{\omega=\omega_0}$ $(m = 0, 1, 2, \dots)$ represents the nth-order dispersion.
Different order terms give rise to diverse pulse characteristics. Furthermore, depending on the material or pulse bandwidth, higher order terms can be negligible. The first terms are more significant and therefore have particular names to describe them. The first order dispersion term is called *group delay* and is defined as:

$$\beta_1 = \frac{1}{v_g} = \frac{n_g}{c} = \frac{1}{c}\left(n + w\frac{dn}{dw}\right) \tag{2.19}$$

where v_g is the *group velocity*, describing the speed of the pulse envelope and n_g is the group index. This quantity is plotted with respect to the wavelength in blue in Figure 2.1. The second order dispersion is called *group velocity dispersion* (GVD) because it represents the frequency dependence of the group velocity:

$$\beta_2(\omega) = \frac{\partial^2\beta}{\partial\omega^2} = \frac{\partial}{\partial\omega}\left(\frac{1}{v_g}\right) \tag{2.20}$$

GVD is responsible for the temporal stretching when the pulse propagates in linear dispersion media and has units of $s\,m^{-1}$. In fiber optics literature is more common to express the GVD dependence in terms of wavelength, defining *dispersion parameter D*:

$$D = \frac{2\pi c}{\lambda^2}\beta_2 \tag{2.21}$$

The sign of the GVD parameter is important because it leads to extremely different physical phenomena for pulses propagating in dispersive media, as described in Figure 2.2.
For $\beta_2 > 0$, the regime is called *normal dispersion*. The name *normal* alludes to the fact that this dispersion is observed in most transparent media in the visible spectral region. In this regime, low frequency components (red) will travel faster than the high frequency components (blue) of the pulse. The variation of the frequency with time within a pulse is called *chirp* and in this case, is called positive or up-chirp. In constrast, in the *anomalous regime* $\beta_2 < 0$, the opposite situation occurs and a negative chirp is induced. The case when $\beta_2 = 0$ is also possible. The wavelength at which this happens is called *zero-dispersion wavelength* λ_D. In silica-based fibers, this value is 1.3 μm. As shown in Figure 2.1, the normal regime is found for wavelengths longer than $\lambda < 1.3$ μm, while for anomalous shorter wavelengths are required.

Another point to define is the propagation distance at which the dispersive effects start to be relevant. This quantity is given by the *dispersive length* L_D, defined by the expression $L_D = \frac{T_0^2}{|\beta_2|}$, where T_0 is the pulse duration. For lengths $L > L_D$, dispersion effects related to temporal stretching are present.

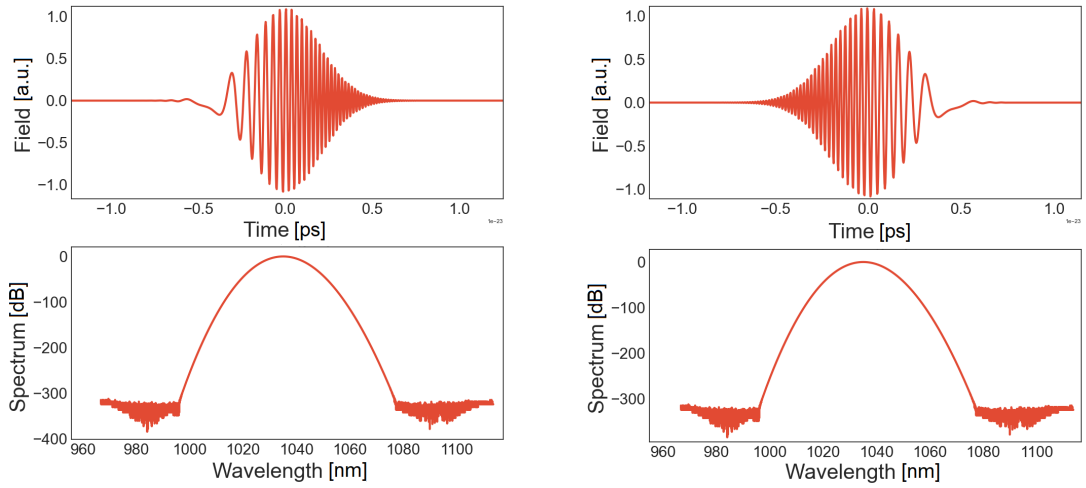

Figure 2.2. *Schematics of the effect of dispersion in an optical fiber (β_2 = 2.4 ps^2/cm) using a gaussian input pulse (T_{FWHM} = 200 fs, P_p = 20 mW) propagating in 10 m of optical fiber. When it passes through the dispersive material, the frequencies below the temporal envelope reorganize depending on the sign of the GVD parameter. (a) For normal dispersion or $\beta_2 > 0$, the red frequency components (leading trail) travel faster than the blue frequency components. (b) For anomalous dispersion $\beta_2 < 0$, the opposite situation happens. This reorganization of frequencies leads to the temporal broadening of the pulse. The spectra of the pulses do not undergo any modification.*

In single mode fibers, dispersion effects are called intra-modal dispersion, and they combine material and waveguide dispersion effects. The plots shown in Figure 2.1 are for bulk fused silica. The effect of a waveguide is to decrease slightly the material index $n(\omega)$ of the core, that is also frequency dependent [14]. Thus, a material contribution has to be added to the net dispersion. This contribution is small except for values around λ_D. The effect of waveguide dispersion is to shift this value to longer wavelengths, $\lambda_D = 1.31$ μm [14].

Polarization mode dispersion

The name single mode fiber can be initially misleading, because a fiber of this type can support the propagation of two orthogonal polarized components of the same mode. In ideal conditions (cylindrical symmetry and stress-free fiber), an optical mode propagating in a particular direction would not couple to the orthogonal mode. However, real life fibers do not present perfect cylindrical symmetry. Deformations during fabrication or induced stress cause anisotropies in the fiber, leading to slightly different propagation constants for both orthogonal directions. This phenomenon is also named *modal birefringence* and it causes the orthogonal polarization components to propagate at different velocities in the fiber [14]. Fibers based on this effect have been developed and are called polarization maintaining (PM) fibers. These fibers have been designed to carry two independent polarization states. The birrefringence control in the fiber is done by inserting rods in the cladding to induce stress in the core. The arrangement of these rods follows different geometries, including bow-tie and PANDA profiles [14]. PANDA design is extensively used in passive and gain fibers because it presents low loss and uniform propagation. PANDA fiber is used for both passive and gain fiber in the laser presented here. PM fibers allow only the light coupled into one of the two polarization axis (slow or fast) to maintain its polarization plane along the fiber length. Any other light coupled in a different angle will not preserve this property.

2.3 Nonlinear effects and pulse propagation equation

In the previous section, the optical effects were described by a linear relation between the electric field and the polarization induced on the dielectric materials. This approximation works well in classical optics, were the electric fields are weak. For higher field strengths, as in pulses generated by femtosecond lasers, the relation is not linear anymore. Moreover, the pulse intensity is further enhanced in optical fibers because light is focused into a small cross section. To observe nonlinear effects, electric fields of the order of $E_c = 5.14 \times 10^{11}\,\mathrm{V\,m^{-1}}$ are required [20].

The phenomenon can be understood by the Lorentz model, which uses a simple oscillator to describe the interaction between the nucleus and electrons in an atom. When an external field is applied, it acts on the center of the electron cloud, displacing it from the center of the positive nucleus, leading to the formation of an electric dipole. Considering that a bulk material is made of a large number of atoms, the sum of all individual dipoles gives rise to a macroscopic polarization. For weak electric fields, the restoring force acting on the cloud electrons depends linearly on its displacement. Contrary to this situation, when the applied field is extremely intense, the restoring force will have a nonlinear term (quadratic, tertiary and so on) that will give rise to the formation of new spectral components.

In this case, the polarization $\boldsymbol{P}$ can be expanded in a power series of $\boldsymbol{E}$:

$$\boldsymbol{P} = \varepsilon_0 \left(\chi^{(1)}\boldsymbol{E} + \chi^{(2)}\boldsymbol{E}^2 + \chi^{(3)}\boldsymbol{E}^3\right) + \ldots \equiv \boldsymbol{P}^{(1)} + \boldsymbol{P}^{(2)} + \boldsymbol{P}^{(3)+\ldots} \tag{2.22}$$

where $\chi^{(i)}$ terms are the ith-order nonlinear susceptibility, in general, a tensor of order $i+1$. Since the optical fibers are made of isotropic and homogeneous materials, these fields are scalar quantities. As mentioned in Section 2.2.1, the linear polarization includes the effects of refractive index and absorption, that for optical fibers is translated into attenuation. The term $\boldsymbol{P}^{(2)}$ represents the second-order nonlinear polarization, $\boldsymbol{P}^{(3)}$ the third-order nonlinear polarization, and so on for higher order terms. In materials with inversion symmetry (invariant under a rotation around a point), $\chi^{(2)}$ vanishes. Examples of these materials are glasses, thus, optical fibers do not show *a priori* any second-order nonlinear effects. Therefore, the main contributions to the polarization in optical fibers will be the linear and third-order nonlinear polarization: $\boldsymbol{P} = \varepsilon_0\chi^{(1)}\boldsymbol{E} + \varepsilon_0\chi^{(3)}\boldsymbol{E}^3$.

2.3.1 Nonlinear propagation equation

In this section, a propagation equation that considers the contribution of the nonlinear polarization will be derived. The approach follows the same derivation steps as in Section 2.2, but the electric displacement is defined here considering the nonlinear polarization term as: $\boldsymbol{D} = \varepsilon_0\boldsymbol{E} + \boldsymbol{P} = \varepsilon_0\boldsymbol{E} + \boldsymbol{P_L} + \boldsymbol{P_{NL}}$, leading to the expression:

$$\nabla^2\boldsymbol{E} - \frac{1}{c^2}\frac{\partial^2\boldsymbol{E}}{\partial t^2} - \frac{1}{\varepsilon_0 c^2}\frac{\partial^2\boldsymbol{P_L}}{\partial t^2} = \frac{1}{\varepsilon_0 c^2}\frac{\partial^2\boldsymbol{P_{NL}}}{\partial t^2} \tag{2.23}$$

The next step is to Fourier transform the equation to the frequency domain to get rid of the time derivatives. Moreover, the expression is simplified by noting that it can be rewritten in terms of the refractive index: $n^2(\omega) = 1 + \chi^{(1)}(\omega)$ and the wave-vector: $k(\omega) = \frac{n(\omega)\omega}{c}$:

$$\nabla^2\boldsymbol{E}(\omega) + k^2(\omega)\,\boldsymbol{E}(\omega) = \frac{-\omega^2}{\varepsilon_0 c^2} FT(\boldsymbol{P_{NL}}) \tag{2.24}$$

The following steps toward the derivation of the propagation equation can be consulted in detail in [14]. The derivation considers the following assumptions:

- The light is propagating in a fixed direction without loss of generality. This property is assured by the waveguide shape. The chosen direction in our study is z.
- No diffraction effects are considered as we are bound in a waveguide.
- The slowly varying envelope approximation (SVEA). This means that the change of the pulse envelope, defined by $A(t) = \left|A(t)\,e^{j\varphi(t)}\right|$, with $\varphi(t)$ a time-dependent phase, when it propagates over a distance equal to one wavelength, is small. We also use PM fibers, so a scalar model is enough to consider in this description.

- The second nonlinear susceptibility term is zero. Only the third-order nonlinear susceptibility is taken into account. This premise is valid in materials with inversion symmetry as silica glass.

Under these assumptions and following the derivation of Agrawal [14], one arrives to:

$$\frac{\partial A}{\partial z} = \sum_{n\geq 2} \beta_n \frac{i^{n+1}}{n!} \frac{\partial^n}{\partial T^n} A - \frac{\alpha}{2} A + i\gamma \left|A\right|^2 \tag{2.25}$$

where A is the complex envelope of the pulse with units $W^{1/2}$, propagating along the direction z, T a coordinate moving with the same velocity as the group velocity v_g of the pulse, β_i is the Taylor expansion of the propagation constant, α is the attenuation parameter and γ the nonlinear parameter. This parameter is proportional to the third order nonlinear susceptibility and describes the strength of the nonlinearity as:

$$\gamma = \frac{3\omega_0}{2n\left(\omega_0\right)c} \chi^{(3)} \tag{2.26}$$

In the discussion of the following sections, a simplification of Eq. 2.27, simply called Nonlinear Schrödinger Equation (NLSE) will be used. In this equation, the effect of the losses is neglected and the propagation constant is approximated to the second order. This is a good estimation since the temporal duration of the pulses is not so short (>5 ps):

$$\frac{\partial A}{\partial z} = -i\frac{\beta_2}{2} \frac{\partial^2 A}{\partial T^2} + i\gamma \left|A\right|^2 A \tag{2.27}$$

The first right term of Eq. 2.27 is related to the dispersion in the fiber, and the second is related the nonlinear phase acquisition. No attenuation term was considered as in 2.25, linked to the losses acquired during the propagation in the fiber.

The mathematical form of Eq. 2.27 corresponds to a parabolic partial differential equation with a nonlinear potential, in the form of a Kerr nonlinearity. This equation can also be found in other physical systems, such as deep-water wave propagation, superconductivity or vortex motions [21]. The second order time derivative is a diffusion term that can have a positive or negative sign and corresponds to the physical situation of the temporal spread or compression of a pulse. This effect can be balanced by the nonlinearity. Some particular solutions to Eq. 2.27 corrrespond to an oscillatory traveling wave with an envelope shaped as a hyperbolic secant that can propagate unchanged (optical solitons).
As it was seen in the case for dispersion, it is worth defining a parameter that help us define the characteristic length at which nonlinear effects are affecting the pulse propagation in a fiber. This parameter is called *nonlinear length* and is defined as: $L_{NL} = \dfrac{1}{\gamma P_0}$, where P_0 is the peak power of the pulse and γ is the nonlinear coefficient previuously defined. For lengths $L > L_{NL}$, nonlinear effects affect the pulse.

2.3.2 Numerical methods

The NLSE is a nonlinear partial differential equation. These kinds of equations often present only a few analytical solutions in special cases [14]. Therefore, different numerical approaches have been developed to find more solutions. In the case of NLSE, the methods typically used are the finite difference time domain method (FDTDM) and the split-step Fourier method (SSFM). As mentioned in [14], SSFM is the standard numerical recipe to model NLSE, and it is the method adopted in this thesis. This method presents numerical limitations, less accuracy and higher number of approximations when solving Maxwell's equations when compared to FDTDM. These disadvantages are not relevant to the type of pulses and cavity design that are being proposed in our study. This section describes the basics of SSFM. A deeper discussion about the FTDTM and the comparison with the SSFM can be consulted in more detail in [14].

Fourier Split-Step Method

When light propagates in a fiber, the dispersive and nonlinear effects act simultaneously. However, in the SSFM, one assumes that these two effects can be thought to act independently over very short fiber lengths. Mathematically, this is represented by separating the effects of dispersion and nonlinearity of Eq. 2.27 in two operators, $\widehat{D}$ and $\widehat{N}$, defined:

$$\widehat{D} = \frac{-i\beta_2}{2}\frac{\partial^2}{\partial T^2} - \frac{\alpha}{2} \tag{2.28}$$

$$\widehat{N} = i\gamma\left|A\right|^2 \tag{2.29}$$

The algorithm divides the propagation medium in slices of equal thickness h. Then, each slice is divided in two sections, as shown in Figure 2.3. In the first slice, the input field $A(z,T)$ is propagated taking into account only nonlinear effects. These effects are represented by the nonlinearity operator $\widehat{N}$, so that at $z = h/2$, the field is $A(z+h/2,T) = \widehat{N}A(z,T)$. To calculate the dispersion effects, it is required to Fourier transform the field $A(z+h/2,T)$ before applying the dispersion operator. Thus, the field at h will be: $A(z+h,T) = \widehat{D}\mathscr{F}\left\{\widehat{N}A(z,T)\right\}$. Since nonlinear effects are computed in time domain, a inverse Fourier transform is performed: $A(z+h,T) = \mathscr{F}^{-1}\left\{\widehat{D}\mathscr{F}\left\{\widehat{N}A(z,T)\right\}\right\}$. This method is sequentially repeated for each slice over the whole fiber length, calculating the nonlinear effects in time domain and dispersion in frequency domain. Since it is required to change back and forth, hence the name Fourier split-step method.
Other modifications to this method are found in literature, as the symmetrized SSFM [14]. In this method, the nonlinearity is considered to act only at the middle of the segment instead than at half the section.

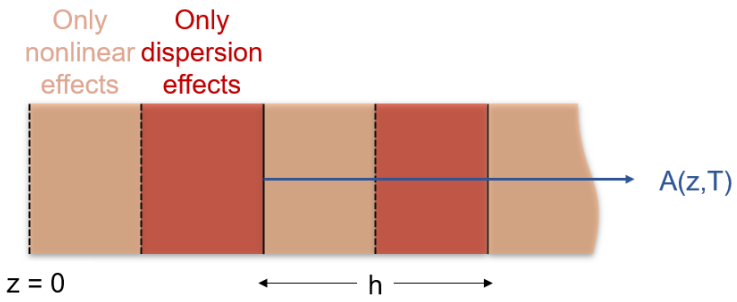

Figure 2.3. *Illustration representing the split-step method. The fiber is sectioned into segments of length h, which in turn are divided again into two parts. Considering that h is very small, the dispersion and nonlinear effects can operate independent of each other. Image adapted from a figure in [14].*

2.4 Nonlinear effects in optical fibers

In the discussion about the origin of the nonlinearities, it was explained that the second-order susceptibility is zero for materials formed by molecules with inversion symmetry, such as silica oxide. Therefore, the first non-zero nonlinear term in optical fibers is the third-order susceptibility. Some of the nonlinear effects that this susceptibility term generates are third harmonic generation, four-wave mixing and nonlinear refraction. In general, nonlinear effects in optical fibers are generated by intensity dependent refractive index because it is more efficient than the frequency-generation effects, as the phase-matching conditions are harder to fulfill in the waveguides.
In this section, a description of the nonlinear refraction or intensity dependence of the refractive index, commonly referred as *optical Kerr effect* will be given. Particular focus will be put on reviewing self-phase modulation, a nonlinear effect caused by the Kerr nonlinearity and relevant to the study of pulse propagation in the proposed laser cavity.

2.4.1 Optical Kerr effect

The optical Kerr effect describes the variation of the refractive index when a high intensity electric field is applied in a nonlinear material with third-order electrical susceptibility $\chi^{(3)}$. It was described previously that in an optical fiber, the total polarization effects can be expressed as $\boldsymbol{P} = \varepsilon_0 \left(\chi^{(1)}\boldsymbol{E} + \chi^{(3)}\boldsymbol{E}^3\right)$. Therefore, the total polarization will present terms oscillating at ω and 3ω, related to the third harmonic generation (THG). An expression for the effective electric susceptibility, can be obtained [20]:

$$\chi_{eff}(\omega) = 1 + \chi^{(1)}(\omega) + \frac{3}{4}\chi^{(3)}(\omega)\left|A\left(\omega\right)\right|^2 \tag{2.30}$$

Thus, the total effective refractive index can be written as $n_{eff}(\omega) = \sqrt{1+\chi_{eff}(\omega)}$. On another hand, if we consider that n_{eff} is the refractive index n_0 with a perturbation caused by the nonlinear contribution Δn as $n_{eff} = n_0 + \Delta n$, then we can equal both expressions:

$$n_{eff}^2(\omega) = (n_0 + \Delta n)^2 = n_0^2 + 2n_0\Delta n + \Delta n^2$$

Considering that $\Delta n << n_0$, the term Δn^2 can be neglected and the following expression is obtained:

$$n_0^2 + 2n_0\Delta n = 1 + \chi^{(1)}(\omega) + \frac{3}{4}\chi^{(3)}|A(\omega)|^2$$
$$\Rightarrow \Delta n = \frac{3}{8}\chi^{(3)}|A(\omega)|^2$$

Therefore, it is possible to arrive to the intensity-dependent refractive index:

$$n_{eff} = n(\omega) = n_0(\omega) + n_2 I(\omega) \tag{2.31}$$

where the Kerr coefficient is given by:

$$n_2 = \frac{3\chi^{(3)}}{8\varepsilon_0 n^2 c} \tag{2.32}$$

On a side note, the nonlinear coefficient defined in Eq. 2.26 can be rewritten in terms of the Kerr coefficient:

$$\gamma = \frac{n_2\omega_0}{cA_{eff}} \tag{2.33}$$

where A_{eff} is the area of the propagating beam in the transverse direction. The units of this coefficient are $m^{-1}W^{-1}$.

2.4.2 Self-phase modulation

A consequence of the intensity-dependent refractive index is the self-phase modulation (SPM). As the refractive index changes, a phase shift proportional to the intensity is induced in the pulse. As the intensity varies with time, the phase is time dependent too, leading to the generation of new frequencies or spectral broadening. The name is coined in reference to the intensity-dependent phase, where a pulse adjusts its own phase. Figure 2.4, shows the propagation of a pulse and a typical SPM spectral broadening.

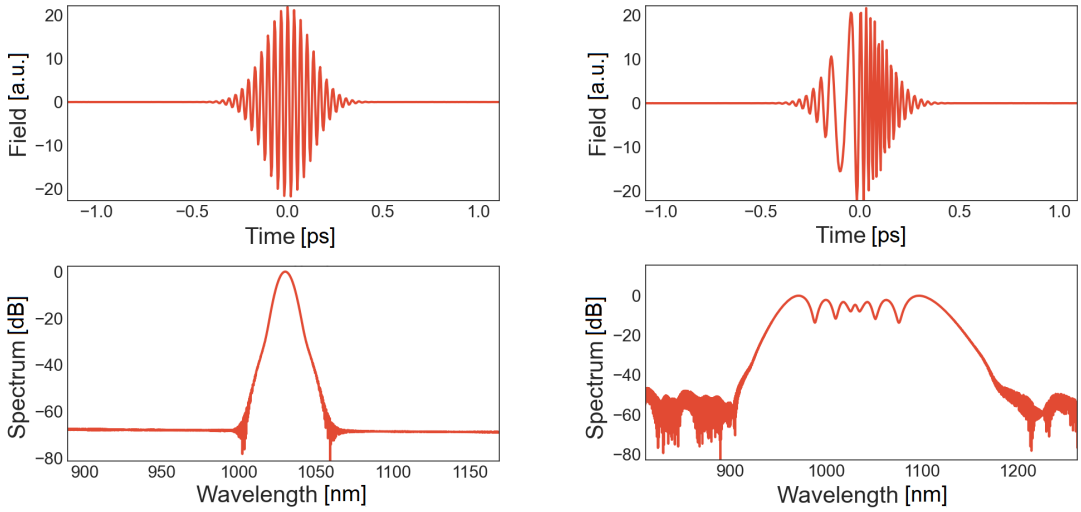

Figure 2.4. *Illustration representing the effects due to SPM in a gaussian input pulse (T_{FWHM} = 200 fs, P_p = 500 W) propagating in 10 m of optical fiber (γ = 0.00387 $(Wm)^{-1}$). (a) Input pulse in temporal and spectral domain. (b) Effects after propagation in a fiber. The temporal envelope of the electric field does not change, but the carrier frequencies under the envelope are reorganized, acquiring a positive chirp, in which the low-frequency components will be found in the leading part of the pulse and the high-frequency components, in the trailing edge. In the spectral domain, SPM forms a modulation of the pulse, leading to spectral broadening.*

A qualitative study of this nonlinear phenomenon can be done by taking Eq. 2.27 as a starting point, where the dispersive effects are neglected (the fiber length is such that $L << L_D$ but $L \approx L_{NL}$, valid for wide pulses in the order of $T_0 > 50$ ps), leading to:

$$\frac{\partial A}{\partial z} = i\gamma \left|A\right|^2 A \tag{2.34}$$

This equation can be solved by separation of variables, as presented in [14], finding that the modulus of the temporal envelope does not change with propagation, ie., $A\left(z,T\right) = A\left(0,T\right)$, where the nonlinear phase acquired by the pulse is proportional to the pulse intensity as a function of time:

$$\varphi_{NL}\left(z,T\right) = \gamma z \left|A\left(0,T\right)\right|^2 \tag{2.35}$$

Time dependent phase is equivalent to spectral broadening, given by δw:

$$\delta w(T) = \frac{\partial \varphi_{NL}}{\partial T} = -\gamma z \frac{\partial \left|A\left(0,T\right)\right|^2}{\partial T} \tag{2.36}$$

Following the definition of the nonlinear coefficient given in Eq. 2.26, the last expression indicates that the spectral broadening depends on the propagation distance, the peak power of the pulse and the pulse temporal duration. As mentioned, the temporal envelope remains unchanged if no dispersion is present. However, the instantaneous optical frequency of the pulse differs from the carrier frequency ω_0. Consequently, the frequency components are readjusted below the envelope, leading to a positive chirp. Thus, the high frequency components (blue) of the pulse are found in the leading edge and the low frequency components (red) in the trailing edge. Figure 2.4 illustrates this situation.

2.4.3 Higher order nonlinear effects

In the discussion of the NLSE, it was mentioned that the nonlinear term is originated by the Kerr nonlinearity. This regime is a good approximation for the proposed cavity, but for ultrashort pulses, other nonlinear effects have to be considered. Some examples include stimulated Brillouin scattering (SBS), stimulated Raman scattering (SRS), or wave-breaking. A more general expresion for the NLSE can be deduced considering the terms that represent each nonlinearity. The mathematical derivation of this expression is far beyond the scope of this text, and can be consulted in [14]. Nevertheless, to have the complete picture of this equation, the generalized NLSE (GNLSE) will be presented:

$$\begin{aligned}\frac{\partial A}{\partial z} - \sum_{n\geq 2} \beta_n \frac{i^{n+1}}{n!} \frac{\partial^n}{\partial T^n} A + \frac{\alpha}{2} A = i\gamma \left(1 + i\tau_{shock} \frac{\partial}{\partial T}\right) \\ \times \left(A \int_{-\infty}^{\infty} R\left(t'\right) \left|A\left(z, T - t'\right)\right|^2 dt'\right)\end{aligned} \tag{2.37}$$

As mentioned, the high order effects are negligible for the frequency comb laser due to several reasons:

- SBS is not relevant for short pulses.
- SRS is relevant for short pulses, but not for pulsed fiber laser cavities, since they have low power and are not extremely long.
- Wave-breaking is observed typically in systems with pulse energy higher than 10 nJ, not the case for the Yb-doped mode-locked fiber lasers.

A relevant note to consider at this point of the discussion are the higher order dispersion effects. During the derivation of Eq. 2.25, a Taylor expansion of the propagation equation was derived where each β_i term was related to the dispersion order. In the discussion that followed, in particular for Eq. 2.27, this expression was approximated to a second order dispersion, because the spectra associated with the pulses simulated in the cavity studied are not broad. In case of ultrashort pulses (<1 ps), the effects of the third-order dispersion, the β_3 term, have to be considered in the Taylor series [14].

3. ANDI FIBER LASERS

As previously mentioned, pulse trains form frequency combs. In mode-locked fiber lasers, pulse formation is based on the balance between the gain, the losses, the dispersion, and the nonlinear effects, whose combination leads to different dynamics and operation regimes [12]. A typical division of fiber lasers is made concerning to the net dispersion of the cavity. The first type is based on a cavity with net anomalous dispersion that balances the positive Kerr nonlinearity. In this case, a fundamental soliton-like pulse is formed [22]. The second case is based on the principle of dispersion-management, in which the cavity is assembled by sections of fiber with anomalous and normal dispersion that compensate for their effects, resulting in a cavity with a small net anomalous or normal dispersion. ANDi (all-normal dispersion) fiber lasers were proposed as an alternative to both cases. In terms of pulse energy, the soliton lasers were limited by the soliton area theorem [23], while ANDi lasers often could yield higher energies of tens of nanojoules [11, 22], one of the main reasons for its future wide-spread development. Besides, this type of laser presents an experimental advantage because its simpler design does not need to compensate for dispersion, a challenge that typically involves adding intracavity free-space elements as prisms, gratings or, chirped mirrors [22].

The first ANDi laser was demonstrated in 2006 [22]. The operative wavelength of the laser was 1 μm, based on a Yb-doped fiber. As it was described in the previous chapter, at this wavelength, the intrinsic dispersion of silica fibers is normal. Due to the positive dispersion, the output pulse is up-chirped, leading to temporal broadening. At the same time, the pulse is also affected by SPM, inducing spectral broadening. The key element in the design was a spectral filter, used to narrow the pulse in both the temporal and spectral domains. This laser mechanism was called *dissipative soliton* because the spectral filter acted as an energy dissipator element, resetting the pulse shape at each roundtrip [12]. Early designs based on spectral filtering included some free-space optical elements [24]. Later on, an all-fiber ANDi laser was achieved, incorporating PM fibers to further improve enviromental stabilization [25]. Future designs explored different saturable absorbers to achieve mode-locking, such as SESAMs [25], nonlinear amplifying loop mirrors (NALM) [26] or giant chirp oscillators (GCO) [12]. The design of the dual-comb presented in this thesis is based on an ANDi configuration in each direction. It brings together the best features of the previous ANDi designs: an all-normal all-PM fiber configuration.

In this Chapter, the concepts to understand the experimental and numerical dual-comb design will be introduced. This discussion will be focused on the single comb, as it represents the first step toward the construction of a dual-comb. First, in Section 3.1, the concept of passive mode-locking, and its relation to the generation of single combs will be reviewed. In the same section, mode-locking mechanisms for dual-combs will be revised. In Section 3.2, an exemplary design to build a single comb will be presented to understand the role of each cavity component. Section 3.3 will focus on describing each cavity component and explaining the equations to numerically model them. At last, in Section 3.4 the concepts explained in the previous discussion will be combined to present the method to perform the simulation of a single comb.

3.1 Mode-locking mechanisms for single and dual-combs

Mode-locking is a technique to obtain ultrashort pulses. In active mode-locking techniques, an external signal is applied to modulate the losses inside the cavity, typically utilizing acousto-optic or electro-optic effects. The second method is called passive mode-locking, and it is based in utilizing nonlinear optical effects such as saturation or refractive index change [27]. Passive mode-locked lasers based on dyes were highly developed in the 70's and 80's, achieving the subpicosecond regime [4]. A decade later, Ti:Sapphire laser was developed, opening the window to the generation of a few femtosecond pulses. The mode-locking technique achieved in this laser was called *Kerr lens mode-locking* (KLM). In combination with an aperture, it worked as a passive saturable absorber. KLM presented limitations on its functionality, mainly related to the self-starting mechanism of the pulses. To start them, a perturbation had to be introduced to the system, often achieved by mechanically tapping the cavity mirrors or by using another absorber, such as dye for example. Semiconductor saturable absorbers with tailorable properties led to a new approach to overcome all these limitations.

Since its discovery in the 90's [4], semiconductor saturable absorber mirrors (SESAMs) have been used to obtain femtosecond pulses. The idea behind saturable absorbers is that the absorption is dependent on the incident light intensity. Briefly described, the pulse intensity distribution has a higher intensity in its center than at the edges. Therefore, after a couple of roundtrips, the low intensity light will vanish. The absorption mechanism can be interpreted as modulation of losses, where low intensity light inside the cavity will be lost. This modulation depends on how fast the absorber recovers. For saturable absorbers (SA) the recovery time is fast, in the order of 1 ps. This allows one to reach shorter pulses than in active mode-locking [28]. The first saturable absorbers were based on dyes. They were hard to manage in the laboratory and had short life. Besides offering an alternative to these disadvantages, SESAMs provided tailored features: wavelength range, absorption recovery time, and saturation fluence [4].

Frequency combs are typically generated by phase-stabilized mode-locked lasers [2]. A schematic spectrum of a frequency comb is shown in Figure 3.1. In the time domain, the mode-locked laser will produce a pulse train with a period equal to the roundtrip time of the pulse in the cavity T_R and a pulse envelope. In the frequency domain, it corresponds to a spectrum formed by narrow optical frequencies with a spacing equal to the repetition rate of the pulse $f_R = 1/T_R$ and a common phase evolution [2, 4].

For single cavity, dual-comb lasers demonstrated so far, not only SESAMs [29] have been used as saturable absorbers. For example, others have used single wall carbon nanotubes (SWNT's) [10, 30]. Lasers based on artificial saturable absorbers as nonlinear polarization rotation (NPR) [11] or a combination of SESAM and NPR [5] have been developed to achieve stable pulses. The latter method has been successful to demonstrate dual-combs, but has required adding free space optics components to control the polarization inside the cavity, as waveplates and polarizers, therefore compromising all-fiber configurations. The first all-fiber, all-PM, Er-doped dual-comb, was demonstrated using a combination of SWNT's with variable attenuators to control the optical losses in both directions [31].

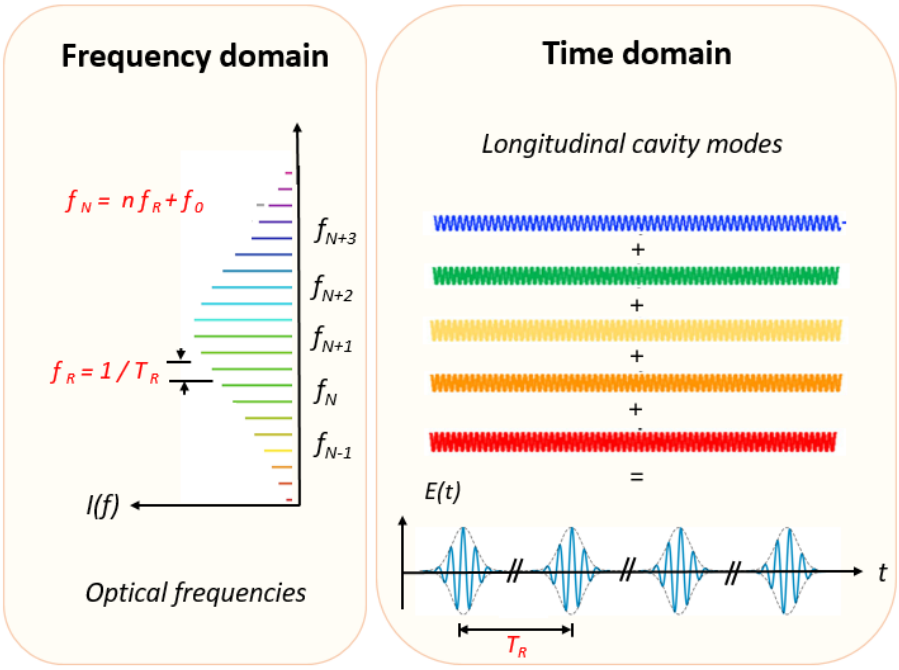

Figure 3.1. *Illustration of the temporal and spectral output of a frequency comb generated by a mode-locked laser. In the time domain, it corresponds to a train of pulses equally distributed in time, where the period T_r is defined by the roundtrip time of the pulse inside the cavity. In the spectral domain, this pulse train is formed by equidistant narrow optical frequencies with a separation given by $f_R = 1/T_r$ and a common phase evolution. Each optical mode is described by $f_N = Nf_r + f_0$, where f_0 is a common offset. The regular separation between the optical frequencies inspired the name in an analogy to a comb. Image adapted from figures in [1, 2].*

3.2 Cavity design of ANDi single frequency combs

Laser cavities can be generally classified in two categories, linear cavities and ring resonators. The feedback system in linear cavities has the typical two-mirror configuration, while ring cavities are closed loops that do not have mirrors at the extremes [32]. The designs proposed for single and dual-comb lasers presented in this thesis are based on ring resonators. In these types of cavities, the repetition rate f_R is given by:

$$f_R = \frac{c}{n_g \times L_{ring}} \tag{3.1}$$

where L_{ring} is the length of the closed ring loop and n_g is the refractive index of the fiber material [33]. The development of optical fiber-based components has made the assembly of fiber lasers easy to perform. For example, the pump light is directed into the cavity by a wavelength division multiplexer (WDM) and its output is directed outside the cavity by an output coupler (OC). Furthermore, in ring resonators, it is possible to get two waves propagating independently in opposite directions (clockwise and anticlockwise).

Figure 3.2 illustrates a simple ring cavity ANDi oscillator using a SESAM as mode-locking element. The cavity consists of normal-dispersion fiber connecting the components. The laser resonator consists of Yb-doped fiber, an OC, and a WDM. A 3-port circulator is used to enable the SESAM coupling and a spectral filter (BPF) resets the shape of the pulse. The output is an up-chirped pulse [22].

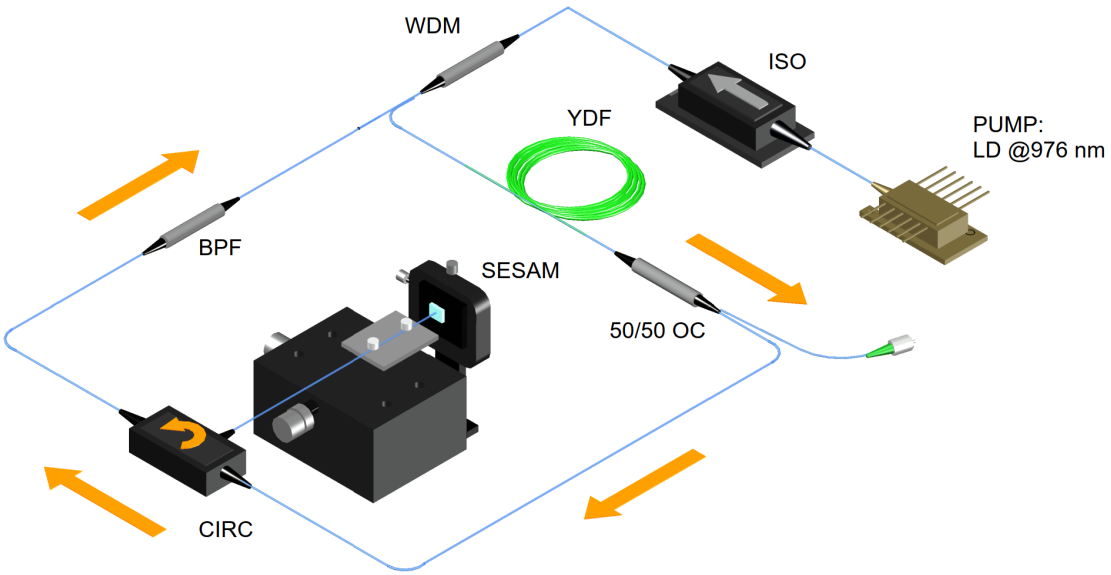

Figure 3.2. *Schematic diagram of a single comb based on Yb. PUMP: laser diode at 976 nm, ISO: isolator, WDM: wavelength division multiplexer, YDF: Ytterbium-doped fiber, BPF: bandpass filter, 50/50 OC: output coupler, CIRC: circulator.*

The evolution of the optical pulse spectrum inside the cavity is shown in Figure 3.3. An input pulse is injected before the gain fiber. After passing through the gain material, the pulse intensity is amplified. While propagating in the passive fiber segments, the spectrum broadens due to SPM, acquiring pronounced cat-ear-shaped edges. The OC couples a fraction of light out, reducing the power. The reflectivity of the SESAM is not perfect, therefore the power is also reduced after this component. The BPF removes the peaks from the spectrum, restarting the pulse shape accordingly to its Gaussian transmission profile.

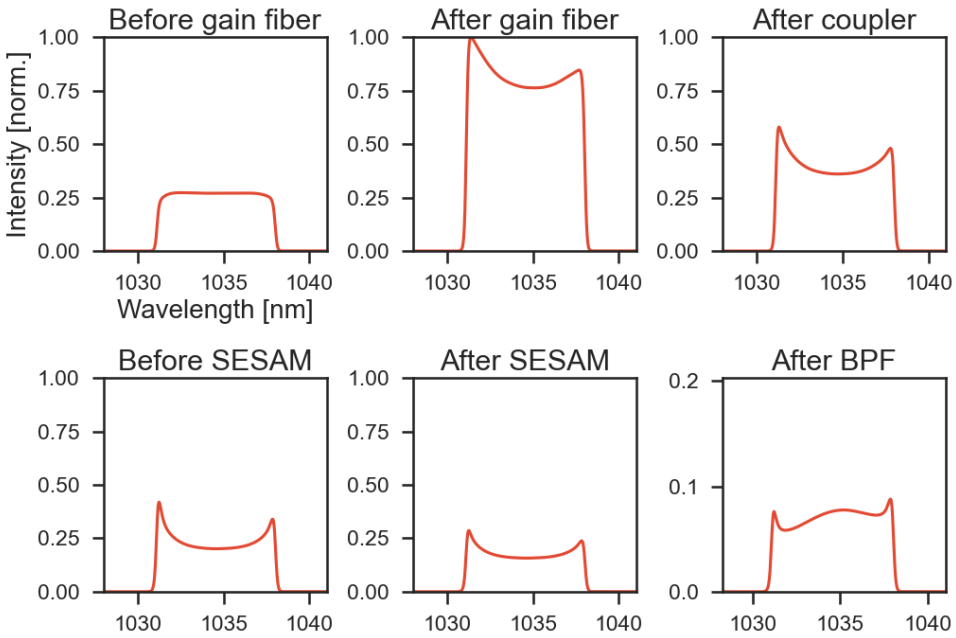

Figure 3.3. *Spectral evolution in an ANDi single frequency comb.*

3.3 Numerical modeling of mode-locked fiber lasers

The numerical simulation of mode-locked fiber lasers is based on modeling separately each oscillator element and sequentially propagating the electric field through them. The following discussion will focus on the physical description and numerical modeling of the Yb-doped gain fiber, SESAMs, and spectral filter. In the last part, the individual models will be combined to form an example simulation of the single comb.

3.3.1 Yb-doped fiber as gain material, simulation by *PyFiberAmp*

In fiber lasers, the amplifying medium is an optical fiber where the core is doped with rare-earth ions. These types of fibers are called *gain fibers*. They set the laser wavelength range of operation, the pump threshold, the conversion efficiency, and the tunability [34]. The most common rare-earth ions used are Erbium (Er^{3+}), Ytterbium (Yb^{3+}), Neodymium (Nd^{3+}), Thulium (Tm^{3+}), Holmium (Ho^{3+}) and Samarium (Sm^{3+}) [13]. These ions have multiple energy levels that lead to transitions in different regions of the electromagnetic spectrum, allowing a broad emission wavelength range. The most used materials are in the near infrared (970 nm for Nd, 1030-1070 nm for Yb) and mid-infrared (2 μm, in the case of Tm and Ho-doped fibers).

Crystals and glasses doped with Yb^{3+} are typical lasing materials for solid-state and fiber lasers. In Figure 3.4 (a) the emission and absorption cross-section of an aluminosilicate fiber doped with Yb^{3+} ions is shown. This type of glass has absorption bands near 915 and 976 nm, therefore it can be easily pumped by popular InGaAs laser diodes, preferring the 976 nm wavelength because it has the strongest absorption. The emission bands are found in the near-infrared, between 950 and 1100 nm, with the maximum gain is at $\approx$ 1035 nm. Since the emission band is broad, Yb^{3+} glass-based lasers can be tunable or used in for ultrashort pulse generation. In Figure 3.4 (b) it is possible to observe the energy-level diagram of this system. As it was previously mentioned, this system is formed by two levels, the ground level ${}^2F_{7/2}$, and a first excited level, ${}^2F_{5/2}$. As it is known, in two-level systems, population inversion is not possible [27]. For this Yb-glass system, the levels are split by Stark effect, forming a quasi-three-level laser at room temperature, allowing the inversion of population required to lase [13, 27].

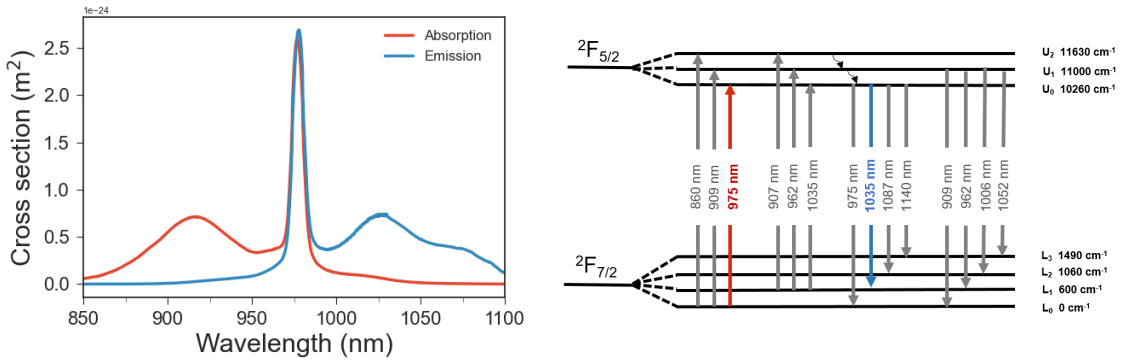

(a) ***(b)***

Figure 3.4. *Ytterbium ion (Yb^{3+}) spectroscopic information. (a) Emission and absorption cross section in aluminosilicate fiber. The maximum absorption peak is at 976 nm, the reason why this wavelength is used as a pump. The maximum gain is the highest at 1035 nm. (b) Energy diagram with the possible transitions between the two-level system of Yb^{3+}. The levels are split due to the Stark effect. Image is adapted from figures in [13].*

To simulate the gain fiber, an open-source library based on Python called *PyFiberAmp* [35] was used. Only a brief explanation about this library will be given, since the details of its implementation are beyond the scope of this thesis, which focuses only on applying it. The library models the gain fiber after the Giles model [36]. This model describes the gain amplification in rare-earth-doped fibers as a two-level system. A system of two equations describing the optical power and the fractions of ions in the excited state form a 1D boundary value problem. The differential equations are solved inside *PyFiberAmp* using the method $solve\_bvp$ from SciPy.

The Giles model possesses some limitations associated with the approximations used on the derivation of the rate equations, such as an averaged dopant distribution or the two-level model itself, that cannot explain more complex transitions. These limitations are not significant to the type of fiber considered in the study. This fiber is *Coherent PM-YSF-HI-HP* and the fiber characteristics, absorption and gain parameters were obtained from the manufacturer.

3.3.2 SESAM as mode-locking element

Semiconductor saturable absorber mirrors (SESAMs) are one of the most used passive components to generate mode-locked lasers [37]. The wide variety of semiconductor materials and growing techniques, such as epitaxy, has provided an extensive selection of devices with tailored properties and characteristics to match the different sets of parameters of the desired laser. One of the typical SESAM configurations is based on reflection, using a Bragg mirror. In this configuration, these devices increase their reflectivity as the input optical intensity increases. Its structure is formed by an alternate series of thin layers made of two different materials with different refractive indices, one higher than the other. Inside the structure, an absorbant layer, typically made of quantum wells or quantum dots, is placed [34]. Low-intensity light is highly absorbed in this layer therefore, less light is reflected or conversely losses are introduced in the cavity. After some roundtrips, this light will vanish. The opposite situation occurs for high-intensity light, where almost all input light is reflected. The mechanism starts from normal noise fluctuations in the CW pump. After some roundtrips, one noise peak will be amplified and will continue to increase its intensity, until a steady state is reached and a pulse train is formed.

Several parameters have been defined to characterize its operation and assure its optimal performance. These parameters are the modulation depth, the non-saturable loss, the saturation fluence, the saturation intensity, and the recovery time. A plot of the reflectivity as a function of the pulse energy fluence in logarithmic and linear scales can be observed in Figure 3.5. In the figure, it is possible to observe how these parameters are defined in the reflectivity curve. Here below, they will be briefly described following reference [37].

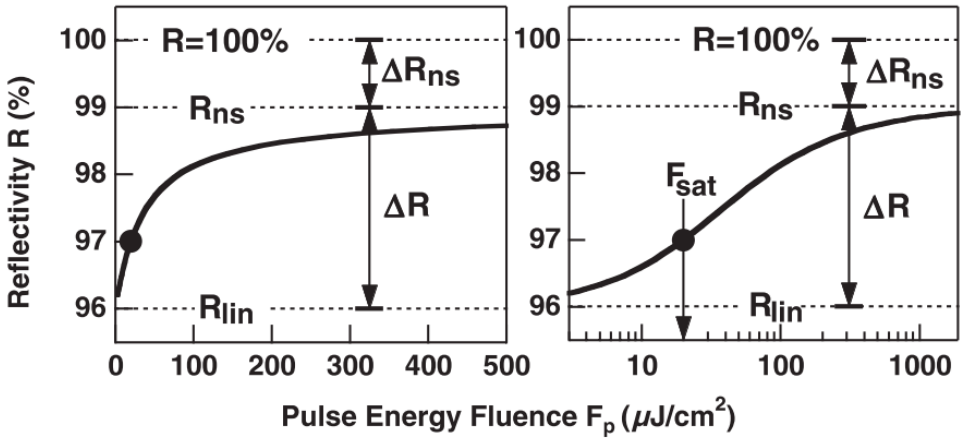

Figure 3.5. *Nonlinear reflectivity curve of a SESAM as a function of the pulse energy fluence in (a) linear and (b) logarithmic scale.* R_{lin} *is the linear reflectivity,* R_{ns} *is the reflectivity with saturation absorption,* ΔR_{ns} *are the non-saturable losses in the reflectivity,* ΔR *is the modulation depth and* F_{sat} *is the saturation fluence. Image is taken from [37].*

Modulation depth $\Delta R\ (\%)$ This parameter is defined as the difference in reflectivity between two characteristic values. The first is when the absorber is completely saturated and reaches its maximum possible reflectivity R_{ns}, and the second, is the maximum value when the absorber operates in the linear regime R_{lin}, expressed as $\Delta R = R_{ns} - R_{lin}$.

Non-saturable loss $\Delta R_{ns}\ (\%)$ It refers to the contribution to the reflectivity losses not related to the absorber itself, being caused by scattering from the interfaces, residual transmission through the Bragg mirror or absorption caused by defects generated during the fabrication of the device. It is defined by the expression $\Delta R_{ns} = 1 - R_{ns}$, where R_{ns} is the maximum value of reflectivity achieved when the absorber is completely saturated.

Saturation fluence $F_{sat}\ (\mu J/cm^2)$ The (pulse energy) fluence $F_{sat} = \dfrac{E_p}{A}$ is the energy of the incident pulse per unit area. The saturation fluence is the fluence required to start the saturation of the absorber. Quantitatively, it is defined as the fluence at which the reflectivity is increased by a $1/e$ (37%) of ΔR with respect to R_{lin} [37].

Recovery time $\tau_{rec}\ (s)$ It is the time the SESAM requires to return to their standard reflectivity level after being saturated by the pulse.

Saturation power $P_{sat}\ (W)$ This is the power required to saturate the absorber. It can be calculated by finding the saturation energy and dividing between the recovery time: $P_{sat} = \frac{F_{sat} \cdot A_{eff}}{\tau_{rec}}$, where A_{eff} is the effective area of the fiber.

SESAM modeling

Due to its semiconductor nature, the SESAM can be modeled as a two-level system, in which the low energy level corresponds to the valence band and the high energy level to the conduction band [34]. Intraband recombinations, trapping, or recombination are neglected. Electrons in the valence band can be promoted to the conduction band by absorbing photons with energy $E = h\nu$. When the absorber is not illuminated, all the electrons are found in the valence band. Once the absorber is illuminated by a laser, the number of electrons in the conduction band increases, until it reaches saturation, that is to say when there are more empty states in the valence band than vacant spaces in the conduction band. These electrons can relax to the valence band by spontaneous emission or non-radiative emission with a relaxation time τ_{rec}. Therefore, the absorption $q(t)$ depends on the number of electrons in the valence band, while the incident photon number depends on the optical intensity $I\left(t\right) = \left|U_i\left(t\right)\right|^2$. This situation can be described by a rate equation for the absorption as a function of time and input field [34]:

$$\frac{dq\left(t\right)}{dt} = \frac{q\left(t\right) - q_0}{\tau_{rec}} - \frac{q\left(t\right)\left|U_i\left(t\right)\right|^2}{P_{sat} \cdot \tau_{rec}} \tag{3.2}$$

where q_0 is the loss coefficient (excluding the non-saturable losses), $\left|U_i\left(t\right)\right|^2$ is the time-dependent power incident on the absorber, $1 - q_0$ is the modulation depth, P_{sat} is the saturation power and τ_{rec} is the SESAM recovery time. This model works well for low fluences as in our experiments. However, in the femtosecond regime, there is a decrement in the reflectivity at higher fluences due to two-photon absorption or thermal effects [37].

3.3.3 Bandpass filter

A bandpass filter (BPF) is an optical device that transmits light in a particular wavelength range. It is characterized by a transmission profile, a central wavelength, and the bandwidth [34]. The BPF used in our experiments has a Gaussian transmission profile:

$$T(\lambda) = t_{\lambda_0} \exp\left(-\frac{1}{2}\left(\frac{\lambda - \lambda_0}{c}\right)^2\right) \tag{3.3}$$

where λ_0 is the central wavelength of the filter, t_{λ_0} is the transmission value at λ_0, and c is the parameter related to the full-width at half-maximum (FWHM), given by $\Delta\lambda_{FWHM}/2.355$, with $\Delta\lambda_{FWHM}$ the filter bandwidth measured at FWHM. The output light after the filter is calculated in the spectral domain, by computing the product of the incident electric field U_i by the filter profile in the spectral domain as in the expression [34]:

$$U_t\left(t\right) = \int_{-\infty}^{\infty} \widehat{U}_i\left(\omega\right) \times \widehat{T}\left(\omega\right) e^{-i\omega t} d\omega \tag{3.4}$$

where U_t is the electric field in time domain transmitted after the filter, $\widehat{U}_i$ is the Fourier transform of U_i, the incident field before the filter and $\widehat{T}(\omega)$ is the filter transmission profile expressed in angular frequency.

3.4 Simulation of a single comb laser based on a ring cavity

This section describes modeling single comb cavities. It serves as a good starting point to understand the dual-comb cavity. The cavity design was already introduced in Section 3.2 and its scheme was shown in Figure 3.2. A schematic representing the method followed to simulate the single comb cavity is shown in Figure 3.6.
The simulation starts with an input field in the shape of a Gaussian or hyperbolic secant pulse. To model the real life amplified spontaneous emission (ASE) variations, random phase and amplitude noise are added. The propagation of the pulse through fiber segments is simulated by solving NLSE (Eq. 2.27) with the split-step Fourier method (SSFM). The gain is simulated by implementing the Yb-doped fiber with the library *Pyfiberamp*, and propagating the pulse by NLSE in the fiber, considering the gain previously computed. The next step to consider is the 50/50 coupler. Its effect can be approximated by a simple scalar multiplication of the field [34]:

$$U_t(t) = \sqrt{R_C} \times U_i(t)$$

where R_C is the coupling ratio into the cavity ($1 - R_C$ in the case out). To model the SESAM, Eq. 3.2 is solved by obtaining the absorption or loss coefficient q over the pulse temporal profile. As with the output coupler, the output field after the SESAM is calculated by the scalar multiplication of the field by the total (saturated) reflectivity, given by [34]:

$$R_{SESAM} = \sqrt{1 - q(t) - \Delta R_{ns}},$$

where ΔR_{ns} is the non-saturated loss of the SESAM. The last component of the ring cavity is the bandpass Gaussian filter. As mentioned before, its effect is obtained by multiplying the spectral transmission profile by the electric field in the spectral domain. This loop is iterated for a determined number of roundtrips, after which a steady output pulse can be formed. Typically, the pulse converges within 600 roundtrips. Convergence depends on the input field shape. Clean pulse shapes result in faster convergence. The field is updated at the start of each loop and the average power is monitored after the output coupler. The effect of the component losses is taken into account by multiplying the output electric field after each element by the linear losses, given by the expression:

$$\mathscr{L} = \sqrt{10^{\frac{IL_{dB}}{10}}}$$

where IL_{dB} is the insertion loss in dB, obtained from the component specification sheet.

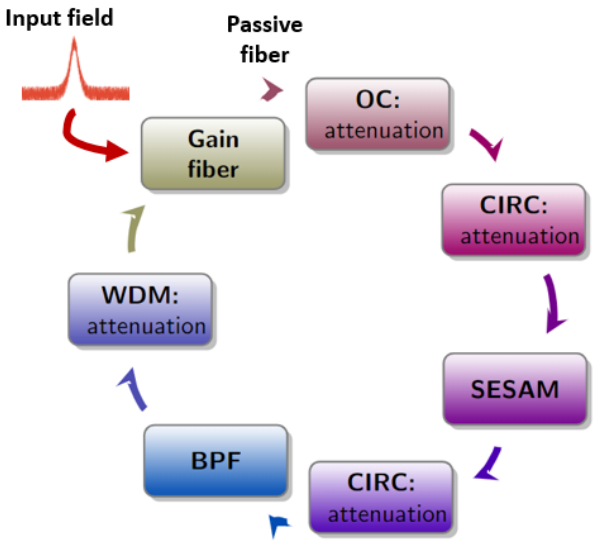

Figure 3.6. *Schematic representing the roundtrip sequence to model a single comb. Each component was modeled independently. An input noisy field is injected before the gain fiber, and the field is updated after each component. A passive fiber segment joins two components. The pulse is propagated in these segments by solving the Nonlinear Schrödinger equation (NLSE) by the split-step Fourier algorithm.*

To complete the description of the simulation, Figure 3.7 illustrates the propagation of a pulse, output of a single comb. The horizontal axis describes the temporal grid where the simulation was defined. In the vertical axis, a projection of the electric field intensity measured at the output coupler for each roundtrip is plotted. During the first couple of roundtrips, the input pulse is noisy. After several tens of roundtrips, the SESAM stabilizes the mode-locking operation and a pulse is formed, propagating stably.

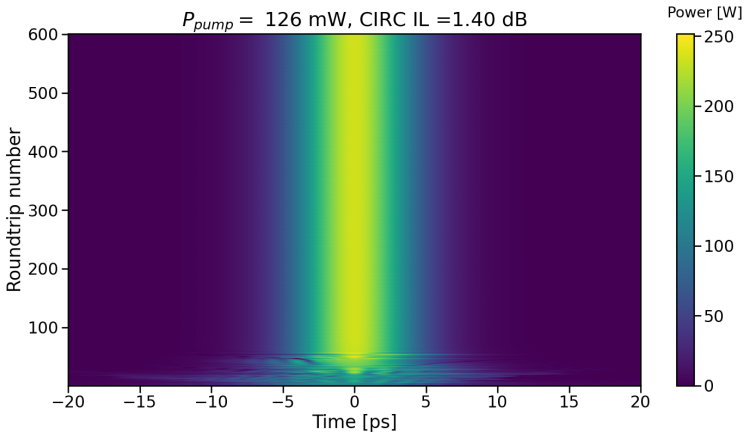

Figure 3.7. *Evolution of the electric field intensity as a function of the number of roundtrips for a single-comb simulation.*

4. RESULTS

4.1 Experimental method

4.1.1 Bidirectional dual-comb fiber laser

Experimental setup

Figure 4.1 shows a schematic of the dual-comb fiber laser. The ring-shaped cavity is build by splicing PM single-mode fiber *(Coherent, PM980-XP, Panda-Type)*. For the gain, an Yb-doped fiber (YDF, *Coherent, PM-YSF-HI-HP, Panda-Type*) is used. The cavity is pumped unidirectionally by a laser diode (LD) operating at 976 nm (*II-VI Inc.*) delivering a maximum output power of 550 mW. A 980 nm isolator (ISO) is used to prevent back reflections from the cavity that could damage the pump diode. The pump is delivered into the cavity by a 975/1030 PM wavelength division multiplexer (WDM) *(OPNETI)*. One 2x2 variable coupler (VC, *Evanescent Optics*) and one 2x2 50/50 coupler (OC, *OPNETI*) are placed symmetrically with respect to the WDM, splitting the cavity into two branches. The other port of each coupler is used to extract pulses from the cavity, and both ends are spliced to two FC/APC connectors that will be connected to different instruments to measure the characteristics of the output pulses. Two three-port circulators (CIRC, *AFR*, *OPNETI*) enable light to circulate in two opposite directions, clockwise (CW) and counter-clockwise (CCW). In both circulators, light propagates from port 1 to port 2 and from port 2 to port 3. A gaussian bandpass filter (BPF) with a central wavelength of 1035 nm and a 7 nm pass bandwidth (measured at 3 dB) is placed symmetrically to the gain fiber. As shown in 4.1, ports 2 of both circulators are butt-coupled to their respective SESAM to achieve mode-locking in each direction. Each SESAM is carefully glued with two-sided tape in a base attached to a kinematic mount. Furthermore, the pigtail is mounted into a horizontal movable base over a 3-axis stage and placed into a fiber holder, where the fiber is held into a groove by two magnetic clamps with a padded base to provide a secure and delicate grip. The coupling between the fiber and the SESAM surface is performed by adjusting the horizontal screw that controls the position of the fiber. To assure correct coupling, the fiber end needs to be cleaved before fixing it in the horizontal base by the magnetic clamps. The correct butt-coupling is achieved when a trasversal bump on the fiber is formed between the clamps due to bending with the SESAM surface.

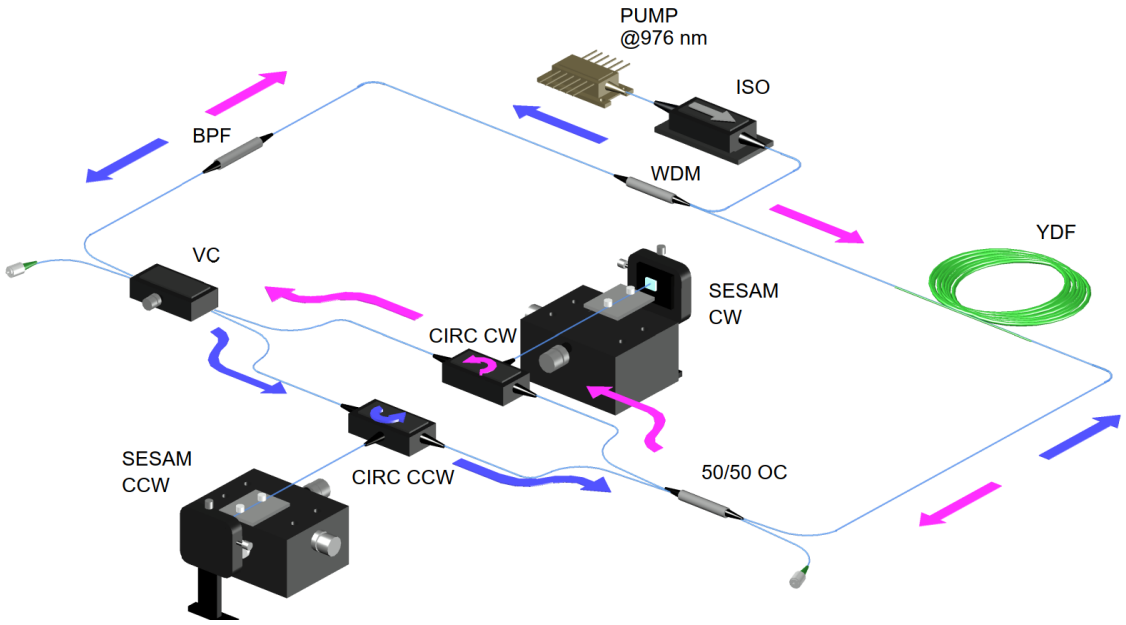

Figure 4.1. *Schematic of a single cavity, dual-comb. PUMP: laser diode at 975 nm, ISO: isolator, WDM: wavelength division multiplexer, YDF: Ytterbium doped fiber, BPF: bandpass filter, 50/50 OC: output coupler, CIRC: circulator, VC: variable coupler, SESAM: semiconductor saturable absorber mirror. In purple, the clockwise (CW) pulse trajectory. In magenta, the counter-clockwise (CCW) pulse. The red box indicates that a modification of the setup was done and the 50/50 output coupler was replaced by a variable coupler.*

Building the dual-comb cavity

The dual cavity was built by assembling two single cavities with a shared path. Following the single comb cavity schematics shown in Figure 3.2, the first step was building the single comb in the CW direction. The second step was to splice the variable coupler and the two FC/APC connectors as in the CW direction of the cavity shown in Figure 4.1. It was verified that the mode-locking train pulses remained, with a slight difference in the repetition rate because of the extra component pigtail fiber. Finally, the CCW arm of the cavity was spliced, including the circulator and SESAM.

The properties of the SESAMs used in the experimental setup are listed in Table 4.1. The critical step while building the single cavities was to find a proper combination of two SESAMs and two circulators leading to stable mode-locked pulses. Both components were chosen taking into account the availability in the laboratory and stability in both directions. Different possibilities were tested independently as single cavities. The most promising combinations were assembled together to form the dual cavity. The variable coupler was initially set at 50/50 ratio, but other combinations were also tried, as it will be discussed in later sections.

Parameters	*SESAM CW*	*SESAM CCW*
Laser wavelength λ (nm)	1040	1040
High reflection band λ (nm)	990-1080	990-1080
Linear reflectivity R_{lin} (%)	84	58
Modulation depth ΔR (%)	11	29
Non-saturable loss ΔR_{ns}(%)	5	13
Saturation fluence F_{sat} ($\mu J/cm^2$)	30	20
Recovery time τ (ps)	1.2	0.8-1
Saturation power P_{sat} (W)	9.40	7.52

Table 4.1. *Properties of the two SESAMs used for building the dual-cavity.*

Characteristics of the two outputs of dual-comb laser

The performance of the output pulses was monitored using an optical spectrum analyzer (*Ando*), two photodetectors (*DET01CFC, Thorlabs*) and a 50 MHz oscilloscope (*Tektronix*). Simultaneous bidirectional comb operation was not achieved. Single comb operation was observed independently to both directions when only the SESAM corresponding to one particular direction was coupled in the cavity. The threshold pump power to mode-lock each direction was 115 mW for CW direction and 96 mW for CCW direction. The mode-locking operation was self-starting, easier to achieve in CW direction than in CCW direction, where tapping the fiber was often required to obtain mode-locked pulses.

To get the best spectral shape for the pulses, the pump power was tuned over a range, while adjusting the SESAM coupling by the kinematic mounts at the same time. Figure 4.2 shows the linear optical spectra measured independently for each direction at the corresponding output ports. In CW direction, for 130 mW of pump power, the central wavelength was 1038.6 nm, the repetition rate was 25.7 MHz, and an output power of 2.2 mW. The corresponding pulse energy is 85.6 pJ. The pulses in the CCW direction with 98 mW of pump power, had a central wavelength of 1038.4 nm, repetition rate of 22.5 MHz and average output power of 1.3 mW, achieving 57.8 pJ of pulse energy. The FWHM is 3.43 nm and 4.06 nm in CW and CCW directions, respectively. The reason why the threshold pump power was lower for the CCW direction has two different origins. In the first place, the SESAM used to achieve mode-locking in CCW direction had less non-saturable losses than in CW direction (5$\%$ and 18$\%$, respectively). The second reason is related to the asymmetry of the cavity. As observed in the experimental setup of Figure 4.1, CW pulses arrive with higher power to the SESAM because they are amplified in the step before, while for CCW, the opposite situation occurs. As a result, CCW direction accumulates higher attenuation. Another consequence of the asymmetry of the cavity and the length of each direction is that the longer path, CCW direction, accumulates more nonlinear phase due to SPM, leading to a broader spectrum.

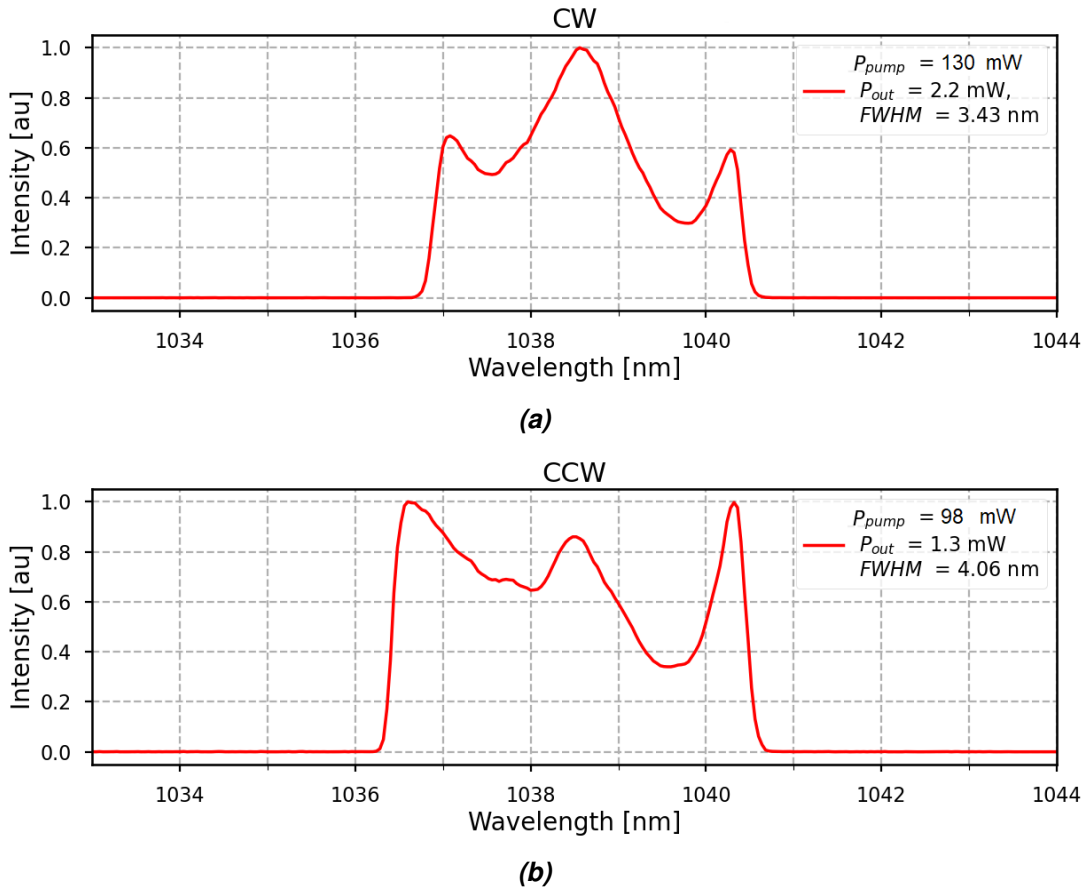

Figure 4.2. *Optical spectra of the mode-locked pulses in CW (a) and CCW (b) directions in the two 50/50 couplers configuration. The spectra were measured independently because bidirectional operation was not achieved. The repetition rate f_R is 25.7 MHz and 22.5 MHz, for CW and CCW respectively. CW direction was easier to mode-lock.*

4.1.2 Variable coupler as a degree of control

The results obtained in the previous configuration highlighted the fact that a more sophisticated loss-gain balance is required in the cavity to achieve bidirectional operation. The default configuration with two couplers set at 50/50 coupling ratio lead to one direction being favored when both SESAMs were coupled. As presented in earlier research on bidirectional lasers [31], independent loss control in both directions has been achieved by introducing a variable coupler before the each saturable absorber. Following this understanding, we varied the coupling ratio of the variable coupler. The target was to increase the coupling ratio to the CCW direction, with fewer losses. However, bidirectional operation was again not attained. The variable coupler had a coupling ratio range between 0 and 100, and because this device was sensitive to backslash, the only way to get the nominal ratio was by measuring the power after the output. Varying the coupling ratio lead to shift in the mode-locking operation from one to the other direction. When the coupling ratio was maximum for CW direction, stable train pulses could be observed, while in CCW no train signal was detected. As the coupling ratio started to change to favor CCW di-

rection, CW train pulses start to lose intensity until they disappear and then mode-locked pulses were observed in the CCW direction. This operation was observed at 115 mW of pump power and it was most of the time self-starting, since sometimes tapping on the fiber was required to observe the train pulses. The repetition rate for CW direction was 22.6 MHz with an average output power of 1.1 mW and for CCW, was 25.5 MHz and average output power of 1.1 mW. The optical spectra obtained for each direction in this configuration is shown in Figure 4.3. Again, the spectral profile corresponds to the steep edges typically observed in ANDi lasers. Then, the pump power was doubled and the coupling ratio was tuned again. However, as the power was increased, it was only possible to observe stable double pulses in a single direction. Comparing Figure 4.2 and 4.3, the spectral shapes and broadening behavior of both configurations are similar for their respective directions, with a small change in the output power due to the coupling ratio.

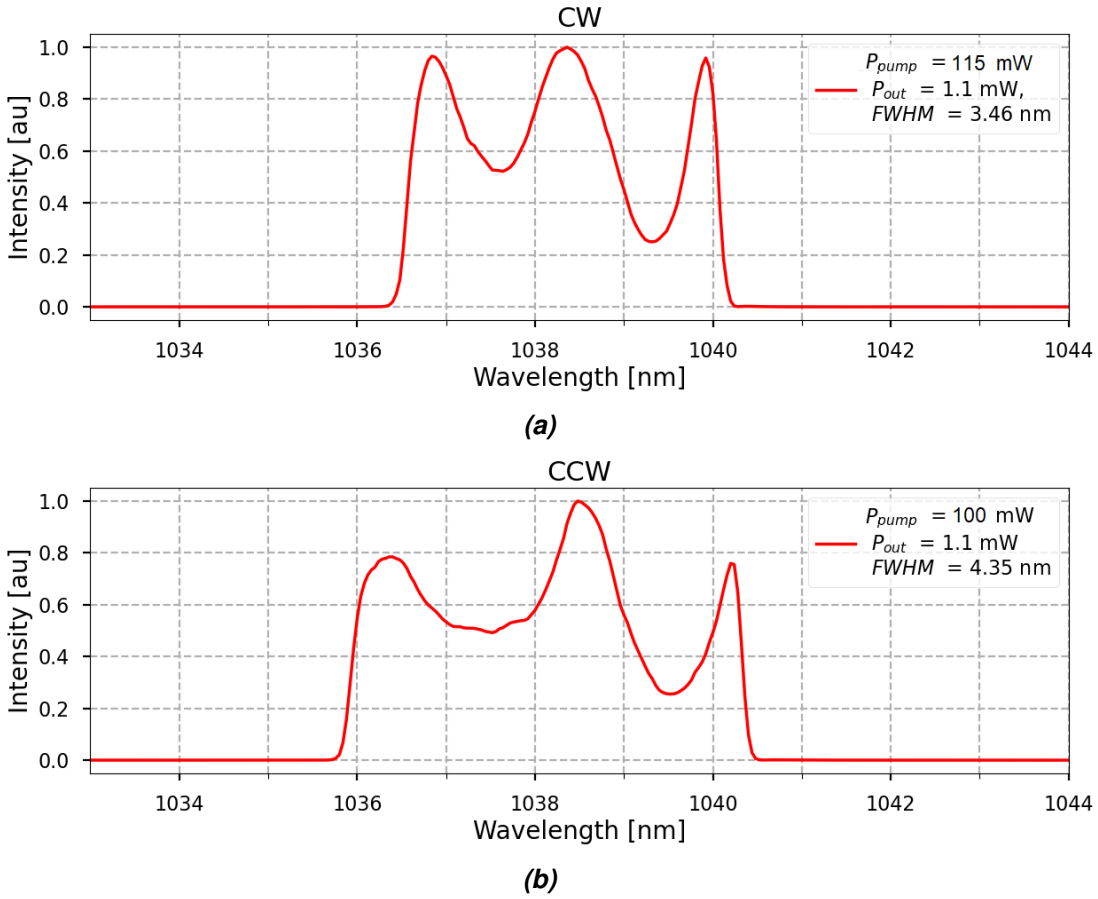

Figure 4.3. *Optical spectra of the mode-locked pulses in CW (a) and CCW (b) directions using a variable coupler. The spectra was measured independently, not in bidirectional configuration. The repetition rate f_R for CW was 22.6 MHz and for CCW was 25.5 MHz.*

Summarizing, independent mode-locked operation was achieved in both directions, but simultaneous dual-comb operation was not successful. To identify and understand the cavity parameters that determine the dual-comb operation, numerical simulations based on the experiments are required.

4.2 Numerical simulations

In the previous chapter, the simulation of a single frequency comb was already discussed. This idea is extrapolated in the single-cavity dual-comb. The dual-comb simulation is fundamentally formed by two single comb cavities with common gain and interaction between the pulses throughout the cavity. Each direction is simulated as an independent cavity following the pulse trajectory indicated by the different colored arrows in Figure 4.1. Therefore, the cavities are the same but traversed in reverse order. The gain is depleted by the average power of both pulses at that location, *ie.*, the gain simulation uses coupled backward and forward signals. Concerning the interaction between the two pulses inside the cavity, the two counterpropagating pulses "collide" during every roundtrip within the common paths of the dual cavity. However, due to the different repetition rates, this point is shifted from roundtrip to roundtrip in the cavity. To keep the model simple, this nonlinear interaction was considered only at four different locations varying from one roundtrip to the other in the CW direction: before the WDM, after the amplification in the gain fiber, after the SESAM, and after the coupler. This interaction was modeled after a simple cross-phase modulation (XPM) term interacting over a fiber length corresponding to the pulse collision time.

Another general aspect considered during the numerical simulations was the configuration of the cavity. Different numerical studies simplify their models by consolidating the total length of the passive fiber and placing it before the gain fiber [38, 39]. During this thesis, it was decided to simulate the passive fiber after each component to reproduce the cavity as similar as possible to the experimental setup.
The input field that was used as seed in both directions of the cavity is a hyperbolic secant pulse with a pulse duration T_{FWHM} = 10 ps. The initial shape is not significant because random phase and intensity noise were added to simulate noise. At each roundtrip, the fields in the CW and CCW direction were saved at the OC position, and the simulation was continued. This algorithm was repeated until the fixed number of roundtrips was completed or when the average power in one direction was smaller than 1×10^{-6} mW. The latter condition prevented cases where only one direction had a pulse and in the other there was only noise, implemented to save computational resources. The number of roundtrips was fixed to 600. This value was found to yield convergence in most cases. The simulations are defined in a time grid formed by 4096 points, using a temporal resolution of 200 ps and a central wavelength of 1035 nm.

A result of the simulation is considered a solution when there are two single pulses with a non-negliglible FWHM propagating in the two opposite directions. A stable solution corresponds to the steady state of our laser system. The criteria to assess whether or not a solution is stable is when it does not change after several hundreds of roundtrips.

4.2.1 Numerical modeling of a bidirectional dual-comb fiber laser

The simulated laser is formed by a Yb-doped fiber segment of 0.75 m and a total passive fiber length of 11.28 m and 8.7 m for the CW and CCW direction respectively, distributed after each component accordingly to the experimental setup. The parameters of the gain, passive fiber, and cavity components can be summarized on Table 4.2. The net dispersion of the laser cavity is estimated to 0.028 ps^2 and 0.022 ps^2 for CW and CCW directions. The insertion losses (IL) of each component were retrieved from their respective specification sheets. The coupling ratio of the output couplers into the cavity is 0.5 and 0.45 for CW and CCW direction, respectively. These components do not include IL. The parameters of the 5 different SESAMs used during the simulations are shown in Table 4.3. These SESAMs were chosen due to their availability in the laboratory.

Gain fiber	*Passive SM fiber*	*WDM*	*CIRC CW*	*CIRC CCW*	*BPF*
β_2 = 0.0024 ps^2/m γ = 0.0038 $(Wm)^{-1}$ A_{eff} = 0.3761 μm^2 L = 0.75 m	β_2 = 0.0024 ps^2/m γ = 0.0038 $(Wm)^{-1}$ A_{eff} = 0.3761 μm^2 L = variable	IL = 0.3 dB	IL = 1.4 dB	IL = 0.8 dB	BW = 7 nm T_0 = 95% IL = 0.3 dB

Table 4.2. *Parameters of the cavity components used during the simulations.*

Parameters	*SESAM 1*	*SESAM 2*	*SESAM 3*	*SESAM 4*	*SESAM 5*
Laser wavelength λ (nm)	1040	1040	1040	1040	1040
High reflection band λ (nm)	990-1080	990-1080	1010-1090	990-1080	990-1080
Linear reflectivity R_{lin} (%)	57	84	54	77	58
Modulation depth ΔR (%)	25	11	36	14	29
Non-saturable loss ΔR_{ns} (%)	18	5	10	9	13
Saturation fluence F_{sat} $(\mu J/cm^2)$	70	30	18	60	20
Recovery time τ (ps)	1	1.2	1.2	3	0.8-1
Saturation power P_{sat} (W)	26.30	9.40	5.64	7.52	7.52

Table 4.3. *Properties of the SESAMs used during our studies. The properties are defined as in Figure 3.5. During the experimental part, SESAMs 2 and 5 were used to build the dual-cavity. During the simulations, all five SESAMs that are listed here were tested.*

The simulation of the single-cavity dual-comb with the parameters previously described for 148 mW of pump power and using SESAM 1 in each direction can be observed in Figure 4.4. In the first row, the evolution of the electric field intensity as a function of the number of roundtrips is shown separately for both directions. The figure demonstrates stable pulses circulating in each direction. The intensity of the input electric field in the time and spectral domains is highlighted in red in the second and third rows for each direction. One can observe that the noisy input field was the same for both directions.

The dynamics of the pulse formation can be described as follows. During the first hundred roundtrips, the intensity builds only in the CW direction. Then, it reaches a state at which the intensity completely disappears in CW and starts in the other direction at full intensity. This behavior lasts for a few tens of roundtrips, until the power is distributed again and the field appears back in the CW direction, leading to a stable propagation of the two pulses in each direction. In the third row of Figure 4.4, the pulse spectral shape at the last roundtrip, for both pulses can be seen. The spectral shape is similar in both directions and the FWHM is 5.60 nm and 6.26 nm for CW and CCW, respectively. Comparing this result with the experiments obtained for the independent dual-comb cavity, it can be noticed that the FWHM was narrower in the experiments than in the simulations. The spectral shape is also different.

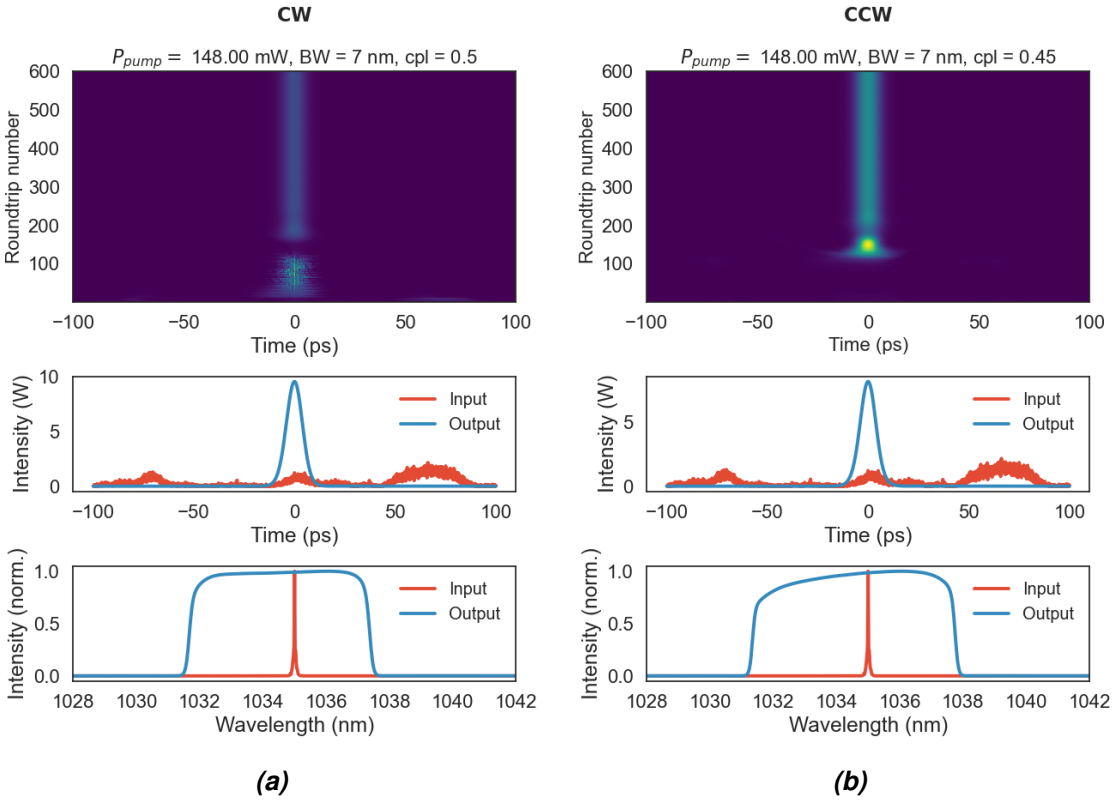

Figure 4.4. *Simulation results show the simultaneous dual-comb operation in CW (a) and CCW (b) for the proposed laser cavity during 600 roundtrips. Top row: Evolution of the electric field intensity as a function of the roundtrips. Middle and bottom row: Temporal and spectral intensity of the input and output electric fields that feed the cavity and were obtained after the output coupler, respectively.*

Another outcome from the previous results is that the IL of the simulated components does not completely match the values of the real components in the case of the WDM and CW circulator. The IL obtained from the specification sheets and the values used in the simulations are listed in Table 4.4. The simulated IL are 40% less than the real values.

Component	*WDM*	*CW CIRC*	*CCW CIRC*	*BPF*
Real *(test data)* IL (dB)	0.5	P1 $\rightarrow$ P2 = 2.26 P2 $\rightarrow$ P3 = 2.33	P1 $\rightarrow$ P2 = 0.84 P2 $\rightarrow$ P3 = 0.75	0.3
Simulation IL (dB)	From 0 to 0.5	P1 $\rightarrow$ P2 = from 1 to 2.2 P2 $\rightarrow$ P3 = 1.4	P1 $\rightarrow$ P2 = 0.8 P2 $\rightarrow$ P3 = 0.8	0.3

Table 4.4. *The insertion losses (IL) of the cavity components. The real values are obtained during the quality inspection each component. For the circulators, P1 $\rightarrow$ P2 and P2 $\rightarrow$ P3 refer to the IL from port 1 to port 2 and from port 2 to port 3. The simulation IL show the ranges tested for each component.*

The reason behind this variation is that when running the simulations with the real IL values, no solution was obtained. An example of this situation is shown in Figure 4.5. The parameters of the simulation that yielded a solution were the same, but the IL of the CW direction circulator was increased to 1.5 dB (increment of 2 $\%$). This simulation leads to different dynamics and does not correspond to a dual-comb solution. The intensity of the pulse in CW direction dies after a few hundred roundtrips, while in the CW direction double pulses propagate stably.

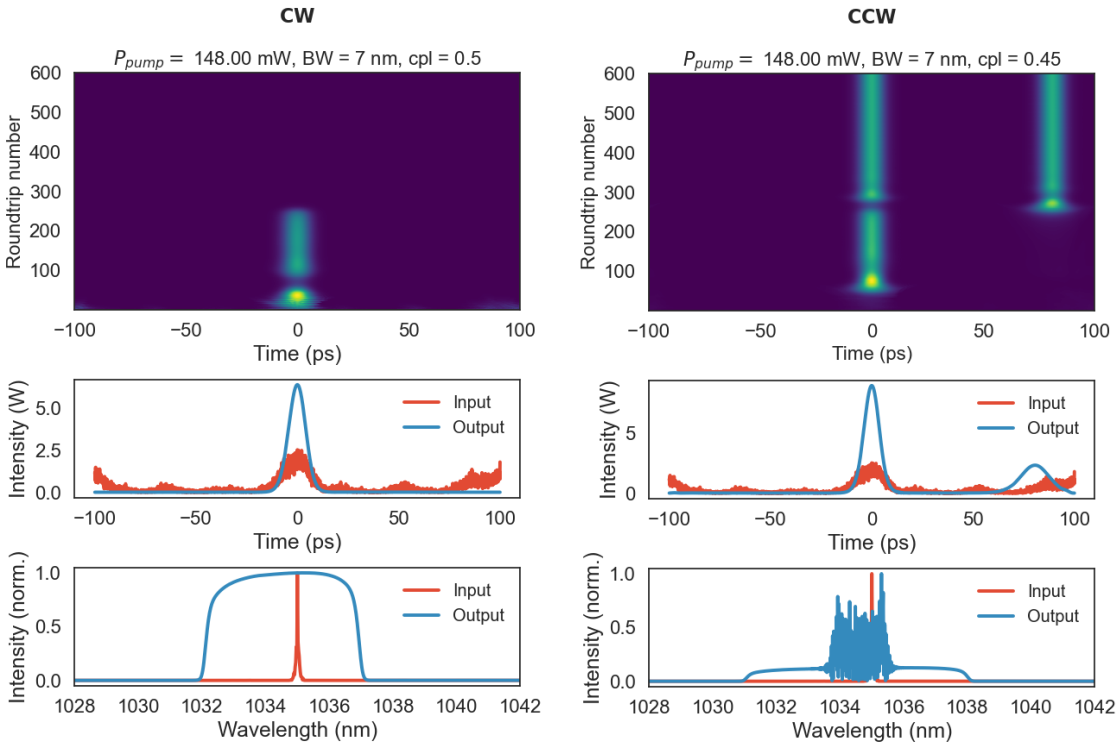

Figure 4.5. *Evolution of the electric field intensity for the CW (a) and CCW (b) directions in a simulated single-cavity dual-comb laser when increasing the CW direction circulator insertion loss from 1.4 to 1.5 dB. This case does not corresponds to a solution of the dual cavity because the single counterpropagating pulses were not formed.*

The motivation of the following three sections is to study and understand the role of the losses of cavity components in the generation of dual-comb solutions. Three different cases will be examined. In the first case, the amount of losses and their position (which component they are tied to) are varied. This will be done by tuning the insertion losses over a range in two components, the CW direction circulator, and the WDM. In the second case, the effect of the SESAM parameters on the gain-losses balance inside the cavity will be studied. Here, cavities formed by two of the same or different SESAMs will be considered. In the last case, the gain coupling and its effect will be analized to compare it with single comb cavities.

4.2.2 Variation of the losses inside the cavity

Variation of the CW circulator insertion losses

To understand how the insertion losses (IL) of the components affect the formation of dual-comb solutions, the IL of the CW circulator from Port 1 to Port 2 was varied, keeping the value from Port 2 to Port 3 fixed at 1.4 dB. This component was chosen because it is present only in one direction of the cavity and has higher IL than the CCW circulator in the experiments. Moreover, CW direction was favored for independent mode-locking operation in the experiments. To understand how the pump power affected the formation of solutions, the range was tuned from 96 mW to 207 mW at 7 mW steps, analogous to the experimental range. The interval of the CW direction circulator IL was chosen from 1.0 dB to 2.2 dB, so that the upper limit corresponded to the real value of the component.

Figure 4.6 shows the results obtained for each direction in a heatmap plot. Each square represents a combination of IL and pump power values that were fed into the simulated cavity. The purple squares highlight the combinations for which a dual-comb solution, *ie.* pulse propagation in both directions, was achieved. In orange are the cases where a double pulse was obtained in one of the directions. In blue are the cases where single pulse operation was achieved only in one direction, as in the experiments. The cases that are not solutions to the dual-comb are colored in lighter color. The metric of the heatmap is the spectral FWHM of the pulse, measured in each respective direction.

The dual-comb solutions are concentrated in a defined area of the heatmap. Due to the random component of the input field, there are convergence variations. For example, when moving along an IL value, in between the solutions there are non-solution squares. This behavior is also observed for the multipulse cases. Therefore, the simulations can be used for qualitative comparison and observation of general trends for each of the three cases to be studied in these sections. A statistical investigation, *i.e.* running several simulations for the same set of cavity parameters, would be required to understand this situation with more detail.

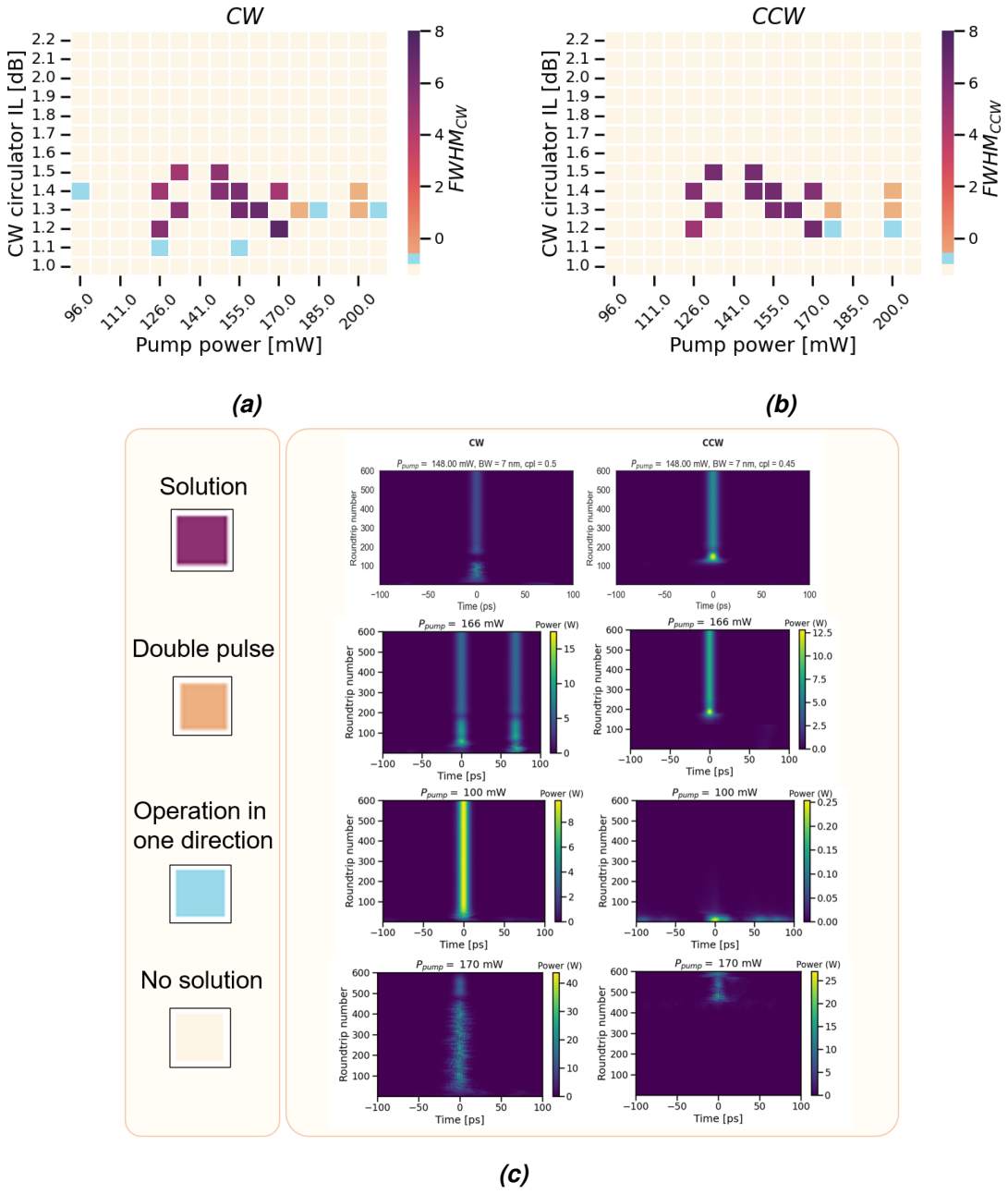

Figure 4.6. *Heatmap plot representing the generation of solutions for the simulated dual cavity when the insertion losses from Port 1 to Port 2 in the CW direction circulator are varied as a function of the pump power. The CW direction circulator IL from Port 2 to Port 3 is fixed at 1.4 dB. (a) Pulse circulating in the CW direction and (b) CCW direction. (c) Color code of the heatmap. Highlighted in purple are the cases where two pulses propagated in the cavity, corresponding to a dual-comb solution. In orange, the cases of double pulse in one direction. In blue, the cases for single pulse operation in only one direction. The cases that are not solutions are colored in beige. The metric of the heatmap was the spectral FWHM of the pulse for each direction.*

Let us discuss now the general trends observed in this simulation. First, CW direction is favored to mode-lock. This direction has more mode-locked independent solutions (blue) compared to the CCW direction. The same situation was observed in the experiments. Regarding the spectral FWHM of each direction, the values are higher for the CCW direction, towards higher values of pump power, trend observed as well in the experiments.

Another aspect of this simulation can be observed by analyzing the position of the CW direction circulator in the cavity. The IL variation in this component has the same function as if an attenuator or variable coupler was placed right before Port 1. If this situation is translated to a thought experiment, adding the attenuator is equivalent to inserting an extra loss in the CW direction. Overall, the low number of dual-comb solutions and the restriction to few IL values suggest the idea that the loss value is determinant to obtain a solution. Moreover, it indicates that the balance of coupled gain and losses inside the cavity is hard to achieve with this design.

Interestingly, no dependence on the insertion losses was observed when simulating single comb systems. Figure 4.7 shows the results of a single comb simulation where the circulator IL were modified over a fixed pump power range. The parameters of the simulation were the same as the ones defined for the CW direction in Figure 4.6 (a). The color code of the heatmap is identical as well. Comparing both figures, is possible to observe a higher number of solutions in the single comb. This simulation supports the idea that the modification of the IL in a single-comb cavity is not a determinant factor to form a single pulse. The differences in simulating a single or dual-comb are the common gain and pulse interaction for the latter. This result will be further explored in Section 4.2.3.

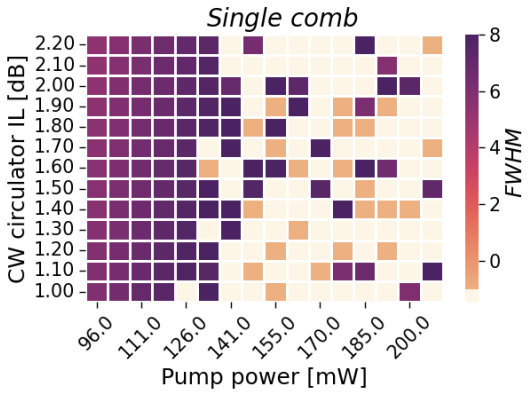

Figure 4.7. *dependence on the circulator insertion losses for a single comb simulation over a range of pump powers. Highligthed in purple colors are the cavity simulations were a single pulse was formed. In orange, double pulse cases. In light color are the cases were no solution was formed. This simulation suggests that single comb simulations are not as sensitive to the variation of the insertion losses as the dual-comb, leading to finding more solutions in the former case.*

Variation of the WDM insertion losses

Compared to only varying the CW direction circulator loss, that only affects one comb, the WDM loss is shared for both components. In this section, the IL of the WDM were varied for a fixed range of pump powers. The IL range spanned from 0 to 0.5 dB, where the upper limit is the value of the component according to the specifications. Following the results obtained in the previous section and without losing generality, the CW direction circulator IL was fixed at one of the convergent values, 1.4 dB. All the other cavity parameters from the previous simulation were kept fixed for this simulation.

In Figure 4.8 a heatmap plot showing the results obtained for this simulation is presented. The color code of the plot is the same as in the previous section. As can be noticed, the WDM IL has more flexibility in the IL variation than the CW direction circulator, showing a higher number of solutions for each IL value. In particular, the first five rows are densely populated, as expected in a situation where the WDM loss does not affect the cavity. Moreover, double pulse cases are more frequent for high values of pump power.

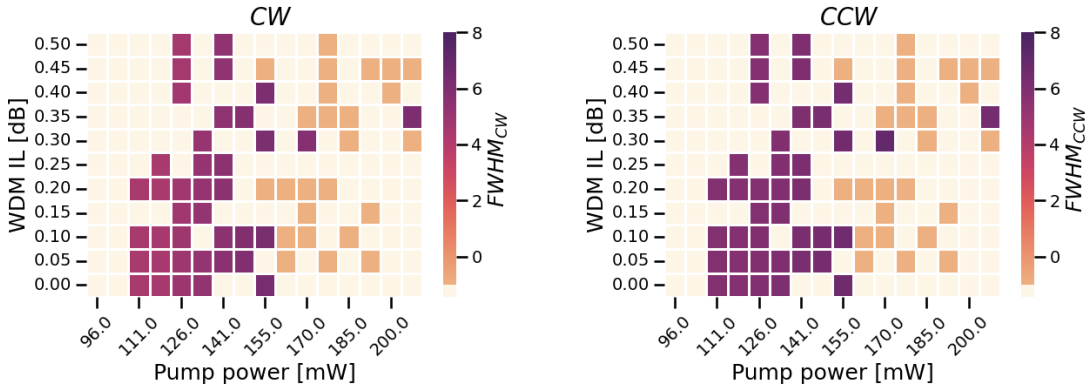

Figure 4.8. *Heatmap plot summarizing the results obtained for the simulation where the insertion losses in the WDM were tuned as a function of the pump power in the dual-comb cavity. (a) Pulse circulating in the CW direction and (b) CCW direction. The insertion loss of the CW direction circulator was fixed to 1.4 dB. Highlighted in purple are the cases for bidirectional operation, ie. one pulse circulating in each direction. In orange, cases where there are double pulses in one direction. In lighter color, the cases that are not a solution to the dual-comb are presented. The metric of the heatmap is the spectral FWHM of the pulse in its respective direction.*

Overall, a higher number of solutions in the WDM simulation means that this component affects less the occurrence of dual-comb solutions. Therefore, combining with the observations made for the CW direction circulator, is possible to conclude that the operation of the bidirectional laser is more dependent on losses that affect only one direction that also change the coupled gain conditions.

4.2.3 Variation of SESAM parameters

In the simulations of the previous section, the pair of SESAMs used in the cavity was kept fixed, *ie.* CW and CCW directions used SESAM 1 from Table 4.1. In this section, the SESAM properties are varied according to the SESAMs available in the laboratory. First, I study the cases where the CW and CCW directions have the same SESAM. The second case considers a combination of two different SESAMs.

Pairs of the same SESAM

The general parameters of the simulated cavity were kept as defined in Section 4.2.1. At each occurrence, the CW direction circulator IL from Port 1 to Port 2 was varied over a range, keeping the IL from Port 2 to Port 3 fixed at 1.4 dB. For each IL value, the pump power was tuned over an interval. The limits for the pump power and the IL were specified similarly as in Section 4.2.2.

The results of this simulation are shown in Figure 4.9. Each figure represents a dual-comb cavity with a different pair of two equal SESAMs. Only the results for the CW direction are shown to highlight the general differences between each pair without focusing in the particular characteristics of its respective simulation. The color code of the heatmap is the same as in the previous section.

As in Section 4.2.2, few values of the IL lead to solutions. The same analogy to a variable coupler can be recovered. In cases where the IL are high, the attenuation of the electric field before the absorption in the SESAM is high as well. In other words, the pulse formation depends on whether its fluence is enough to saturate the SESAM. As described in Section 3.3.2, the parameter that measures this quantity is the saturation fluence F_{sat} of the SESAM. A trend can be inferred in Figure 4.9. Cases with dual-comb solutions for low values of IL correspond to SESAMs with high saturation fluence, as in SESAMs 1 and 4, which have values of 70 and 60 $\mu J/cm^2$, respectively. Conversely, SESAMs 3 and 5 present solutions at high IL and have low saturation fluence values, 18 $\mu J/cm^2$ and 20 $\mu J/cm^2$. SESAM 2 is not considered in the discussion because no dual-comb solutions were obtained.

It can be concluded that equal pairs of SESAMs with low saturation fluence lead to convergent solutions at higher values of the IL. This situation is more approximate to the IL values of the experimental cavity components. This feature is interesting from an experimental point of view. Low saturation fluence SESAMs have the advantage of starting mode-locking at low power level. This helps to prevent the degradation of the device, the main downside for the long term of this passive mode-locking element.

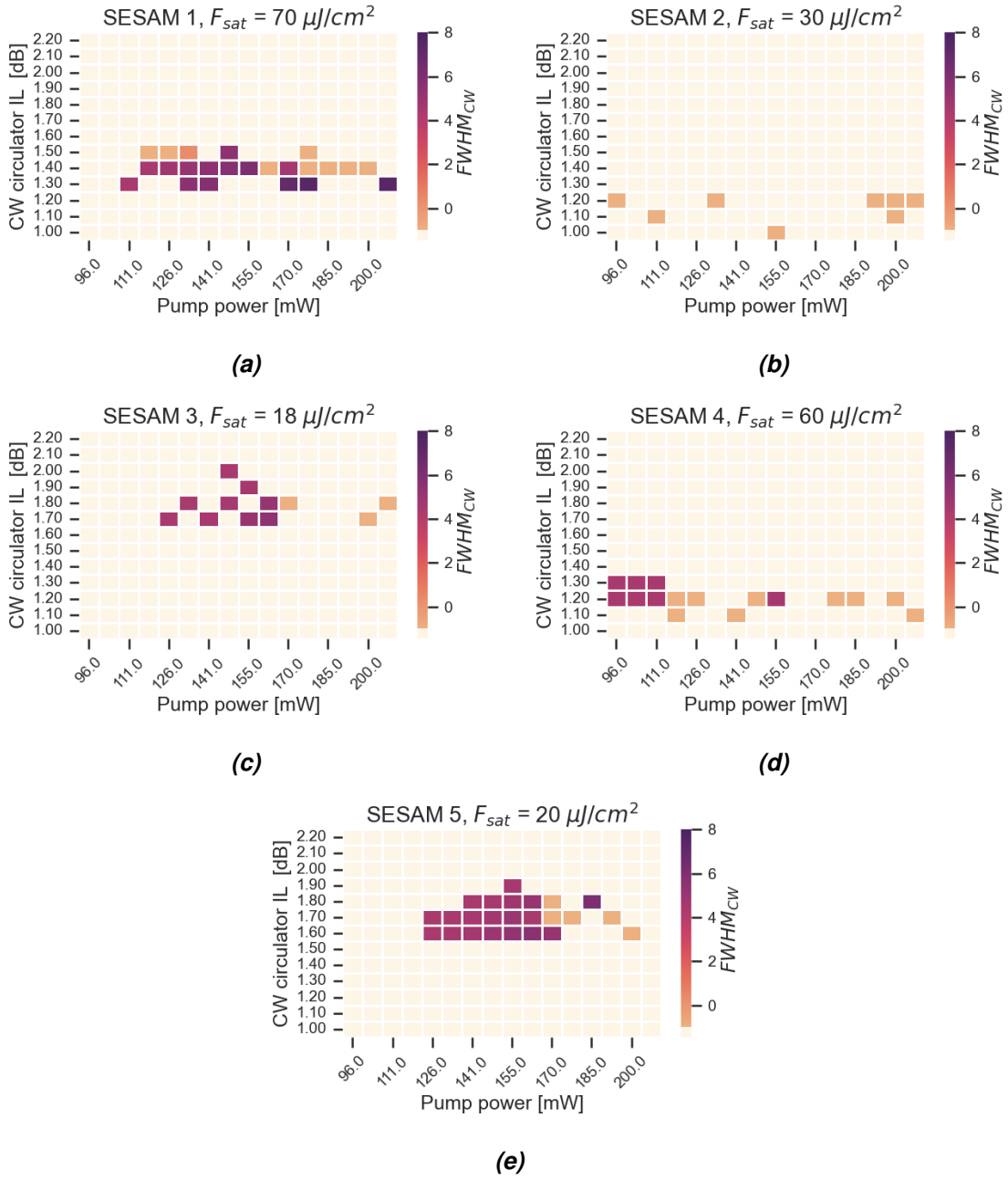

Figure 4.9. *(a-e) Heatmap plots presenting the results obtained in a simulation where the IL in the CW direction circulator are tuned a fixed pump power range. Each plot represents a cavity configuration with a different pair formed by two equal SESAMs. The saturation fluence F_{sat} of each pair is found to be a determinant parameter in the occurrrence of solutions. Lower saturation fluence leads to convergent solutions for higher values of the insertion losses. This situation resembles the experimental cavity conditions.*

Pairs of different SESAMs

To complete the picture of the occurrence of solutions when the pairs of SESAMs are varied, a simulation with pairs formed by two different elements was investigated. Twenty combinations of SESAMs were examined, without considering the pairs formed by equal SESAMs. To reduce the computational effort, only two values of the CW direction circulator IL were considered, 1.3 dB and 1.4 dB. These cases were chosen because they led to convergent solutions in previous cases. For each SESAM pair, the pump power is tuned over the range 96 mW to 207 mW, in steps of 7 mW as in previous cases.

The results are plotted in Figure 4.10. Each figure represents the value of the CW direction circulator IL that was kept fixed inside the cavity. Due to the number of simulations, the pump power value at which the solutions were obtained is not relevant, therefore the pump power information is not shown. The combinations that lead to convergent cases are highlighted in blue and labeled accordingly, while the non-convergent cases are colored in red. Only two combinations were obtained for each insertion loss value. This could also explain problems in the experiments, as two different SESAMs do not seem to lead to dual-comb solutions.

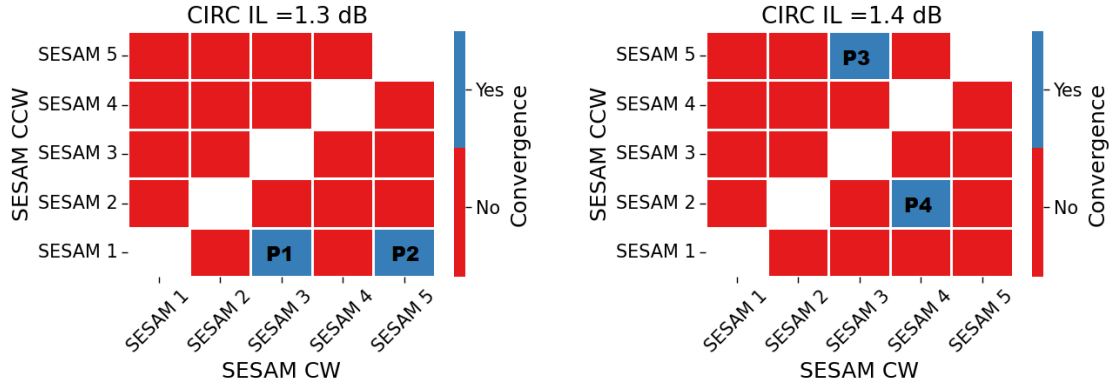

Figure 4.10. *Plot showing the combination of SESAMs that led to solutions of the dual cavity. Each pair is formed by two different SESAMs, forming 20 different combinations. The insertion losses of the CW direction circulator were kept fixed at the values of 1.3 dB (a) and 1.4 dB (b). Highlighted in blue are the cases where a combination of SESAMs, for any pump power in the range, led to dual-comb solutions; in red are the cases with no solution. The legend P is used to label the pairs that led to solutions.*

A common feature of the pairs P1 to P3 is that the non-saturated loss ΔR_{ns} is lower for the CW direction than for CCW. Analyzing the simulation, it can be observed that by design, the CW direction has more losses due to the lossy circulator. Therefore, it would be reasonable to expect a SESAM with low ΔR_{ns} in this direction. Lower loss values favor mode-locking in that direction [29]. The pair P4 does not seem to follow that trend.

4.2.4 Uncoupled gain

Finally, a question remains regarding the effect of the variation of the IL when the gain is uncoupled. Two different situations were tested. The first is presented in Fig. 4.11. The first row describes a dual-comb solution found in Section 4.2.1. The input parameters of this cavity were 126.00 mW of pump power and 1.3 dB in the IL in the CW direction circulator. SESAM 1 was used in both directions. Afterward, a cavity with identical parameters was simulated, but this time uncoupling the gain. This was done by setting the average power in one direction to zero when calculating the gain in the other direction in *PyfiberAmp*. Additionally, the pulse interaction between the two pulses was not considered. The results are presented in the second row. The solution obtained corresponds to two independent single comb cavities in double pulse operation. Another observation is that when the gain is uncoupled, the net gain in the cavity is roughly doubled in each direction, leading to an increase in the available average power. This explains the occurrence of two pulses in each direction. In the third row simulation, the loss parameters were kept fixed but the pump power was decreased to 74 mW. In this case, the double pulses were removed and two independent single pulse combs were obtained in each direction. This effect is similar to the one observed in Fig. 3.2 where double pulse cases are obtained for high values of the pump power. This double pulsing is also typical in experiments with high pump power. Finally, the effect of modifying the losses is shown in the last row. As it would be expected from the results of the single comb from Fig. 3.2, there was no change compared to the previous step. In other words, as the gain is uncoupled the CW and CCW directions operate independently and are not sensitive to IL.

To discard that the results obtained were independent of the order in which the modifications to the dual-comb solution were applied, the same procedure was repeated in reverse. This means that a dual-comb solution was modified to obtain a no-solution case and then the gain was uncoupled. The results are presented in Fig. 4.12. The top row simulation is the same as in Fig. 4.11. In the second row, the simulation where the IL of the CW direction circulator was changed to 1.7 dB, obtaining a non-convergent case. In this situation, no pulses were built in CW while two pulses steadily were propagating in CCW. Subsequently, the gain was uncoupled following the same procedure. The simulation corresponds again to two independent single combs. The results mirror the ones obtained in the same row of Fig. 4.11. As before, uncoupling the gain leads to double the available gain in every single cavity, leading to more power and double pulses in each direction. As next step, the input power was decreased, keeping the IL constant. Again, two independent stable single pulses were obtained in each cavity. This result is the same as in the first case, indicating that the order of the loss modification is not relevant. Therefore, in a dual-cavity where the gain is uncoupled for both directions, the variation of the IL does not affect the convergence of solutions as in the single comb simulations.

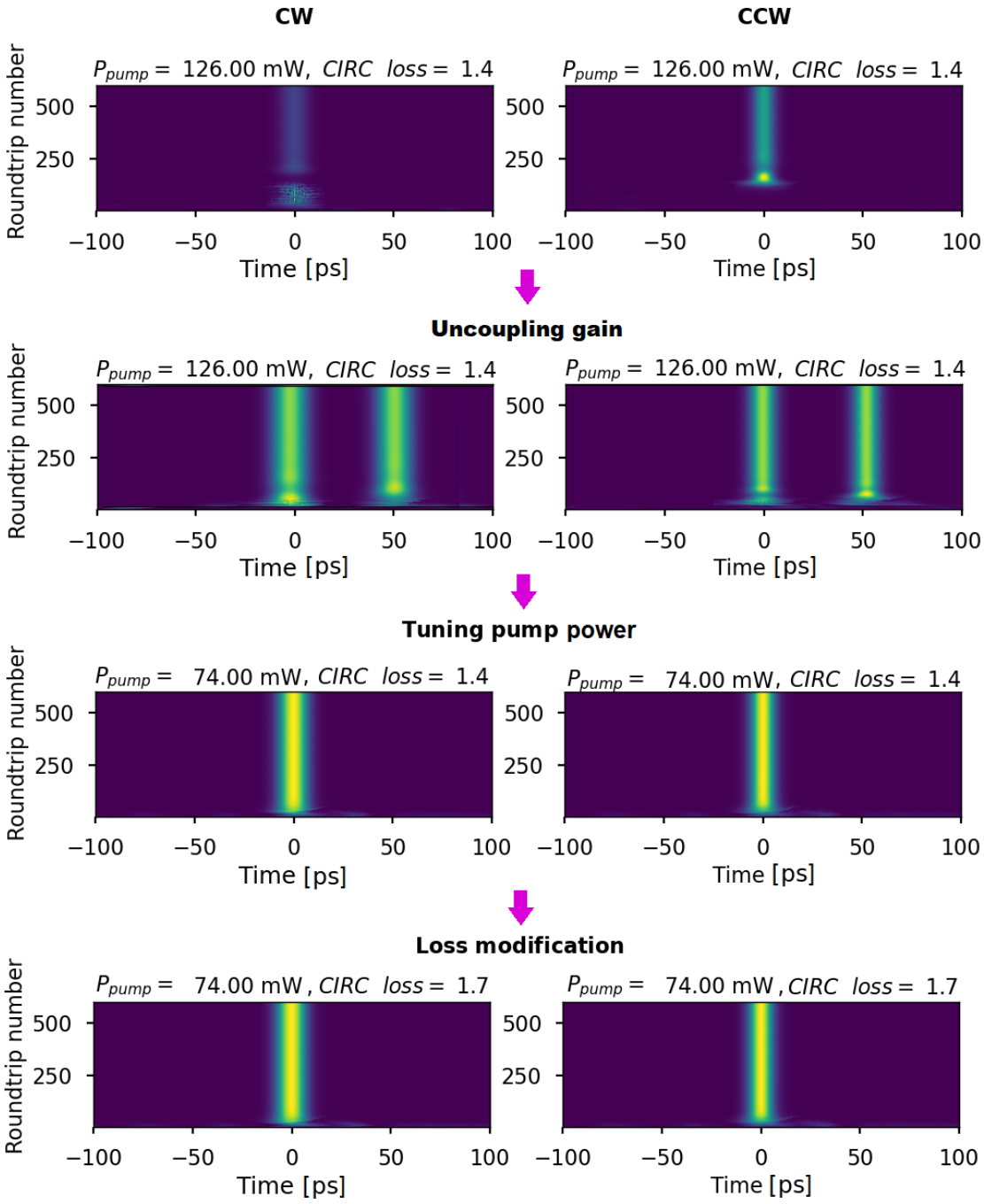

Figure 4.11. *Sequence of simulations performed to study the generation of solutions when the gain was uncoupled in the dual cavity. Top row: Solution obtained in Section 4.2.2.1. Second row: Keeping the same parameters, the gain was decoupled, obtaining double pulses in independent single cavities. Third row: The pump power was decreased, obtaining single pulse operation in each independent cavity. Bottom row: The IL was modified, maintaining the single comb operation as the previous case. When the gain is uncoupled in a dual cavity, the variation of the IL does not affect the convergence of solutions, analogously as in the single comb simulations.*

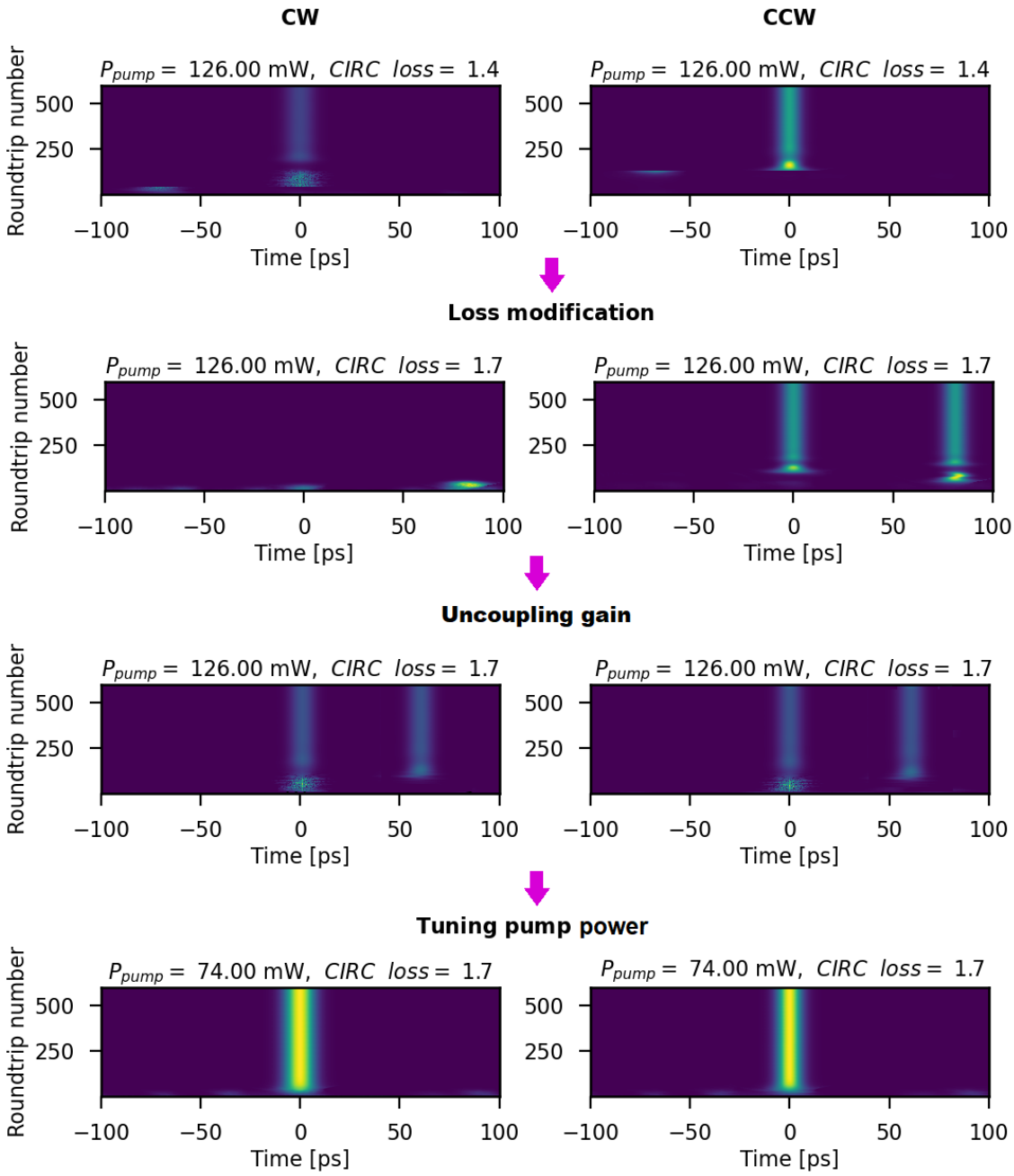

Figure 4.12. *Results obtained when performing a series of simulations to understand the generation of solutions when the gain is uncoupled in a dual-comb. The same modifications were performed as in 4.11, but in reverse order. Top row: Solution. Second row: the IL was modified to 1.7 dB, not a solution. Third row: Simulation when the gain was uncoupled, keeping the values of the previous row constant. Two double pulses are formed in each independent cavity. Bottom row: Decreasing the power leads to two independent single combs. The simulations support the affirmation that the variation of the losses does not affect the convergence of solutions in a single comb results.*

5. SUMMARY AND CONCLUSIONS

In this thesis, the results of an experimental and numerical study of a cavity design for an all-normal all-PM fiber single cavity dual-comb laser have been presented. The dual-comb design was bidirectional operation, with two 3-port circulators to allow independent propagation of the two pulses in opposite directions. The mode-locking mechanism was a pair of SESAMs, one to mode-lock in each direction. Experimentally, mode-locked operation was achieved to both directions independently. However, the simultaneous dual-comb operation was not possible. The experiments suggested that the balance of gain and losses inside the cavity required a more elaborated scheme.

Simulations were performed to investigate the possible issues in the design affecting the simultaneous dual-comb operation. The cavity was simulated matching the experimental design. During the simulations, it was noted that the generation of solutions to the dual-cavity (*ie.* stable propagation of two pulses in CW and CCW directions) depended on the insertion losses of two particular components, the WDM and the circulator in the CW direction. Therefore, three different situations were designed to study how the component losses affected the generation of solutions. First, the variation of the amount and position of the losses was investigated. This was done by tuning the IL of the CW direction circulator and WDM over a pump power range. I obtained that the system was more sensitive to the CW direction circulator insertion losses, because fewer solutions were attained. This result implied that the system might be more sensitive to the losses affecting only one direction. The second situation was to modify the pair of SESAMs used in the dual-cavity. Two cases were considered, one with pairs formed by two equal SESAMs, and the second with pairs formed by different SESAMs. It was found that cavities the same SESAM in both directions, having low saturation fluence values, led to solutions at higher loss values. These cases resembled better the experimental conditions. In the case of pairs formed by different SESAMs, few solutions were found, suggesting that a given pair has a low chance to lead to a solution. The last situation investigated the effect of loss variation in the generation of solutions when the gain in the dual-comb was uncoupled. Uncoupling the gain was analogous to having two independent single combs. It was found that the variation of the losses in the CW direction circulator did not impact the generation of solutions in an uncoupled dual-comb, as in the case of single comb cavities.

A result obtained in the simulations is that the dual-comb design is particularly dependent on the CW circulator loss. Moreover, this dependence was characteristic of the dual-comb, and was not observed in single comb cavities. The simulations suggest that one of the reasons why the experimental dual-comb was not achieved might be due to the imbalance of the losses and coupled gain inside the cavity. The other reason might be due to utilizing different pairs of SESAMs in CW and CCW directions.

Regarding the experiments, future steps include testing a cavity variation that includes two variable couplers or attenuators before each SESAM, following a design presented before [31]. This design allows having independent losses in each arm. Concerning the numerical work, more thorough simulations need to be performed. One of the improvements is to remove the variations in solutions due to random input field together with a more resourceful code to optimize the computational resources. More numerical and experimental work will be required to obtain a better understanding of the requirements to successfully achieve dual-comb operation.

REFERENCES

[1] Picqué, N. and Hänsch, T. W. Frequency comb spectroscopy. eng. *Nature photonics* 13.3 (2019), pp. 146–157. ISSN: 1749-4885.

[2] Fortier, T. and Baumann, E. 20 years of developments in optical frequency comb technology and applications. eng. *Communications physics* 2.1 (2019). ISSN: 2399-3650.

[3] DeMaria, A. J., Stetser, D. A. and Heynau, H. Self mode-locking of lasers with saturable absorbers. *Applied Physics Letters* 8.7 (1966), pp. 174–176. DOI: 10.1063/1.1754541. eprint: https://doi.org/10.1063/1.1754541. URL: https://doi.org/10.1063/1.1754541.

[4] Keller, U. Recent developments in compact ultrafast lasers. eng. *Nature (London)* 424.6950 (2003), pp. 831–838. ISSN: 0028-0836.

[5] Nakajima, Y., Hata, Y. and Minoshima, K. High-coherence ultra-broadband bidirectional dual-comb fiber laser. eng. *Optics express* 27.5 (2019), pp. 5931–5944. ISSN: 1094-4087.

[6] Coddington, I., Newbury, N. and Swann, W. Dual-comb spectroscopy. eng. *Optica* 3.4 (2016), pp. 414–. ISSN: 2334-2536.

[7] Ideguchi, T., Nakamura, T., Kobayashi, Y. and Goda, K. Kerr-lens mode-locked bidirectional dual-comb ring laser for broadband dual-comb spectroscopy. eng. *Optica* 3.7 (2016), pp. 748–. ISSN: 2334-2536.

[8] Link, S., Maas, D., Waldburger, D. and Keller, U. Dual-comb spectroscopy of water vapor with a free-running semiconductor disk laser. eng. *Science (American Association for the Advancement of Science)* 356.6343 (2017), pp. 1164–1168. ISSN: 0036-8075.

[9] GmbH, M. S. *Dual comb spectroscpy*. 2022. URL: https://www.menlosystems.com/applications/all/spectroscopy/dual-comb-spectroscopy/ (visited on 10/15/2022).

[10] Kieu, K. and Mansuripur, M. All-fiber bidirectional passively mode-locked ring laser. eng. *Optics letters* 33.1 (2008), pp. 64–66. ISSN: 0146-9592.

[11] Li, B., Xing, J., Kwon, D., Xie, Y., Prakash, N., Kim, J. and Huang, S.-W. Bidirectional mode-locked all-normal dispersion fiber laser. eng. *Optica* 7.8 (2020), pp. 961–. ISSN: 2334-2536.

[12] Erkintalo, M., Aguergaray, C., Runge, A. and Broderick, N. G. R. Environmentally stable all-PM all-fiber giant chirp oscillator. eng. *Optics express* 20.20 (2012), pp. 22669–22674. ISSN: 1094-4087.

[13] Meyer, J., Sompo, J. M. and Solms, S. von. *Fiber Lasers: Fundamentals with MATLAB® Modelling*. eng. Milton: CRC Press, 2022. ISBN: 0367543486.

[14] Agrawal, G. and Agrawal, G. P. *Nonlinear Fiber Optics*. eng. Optics and Photonics. United States of America: Academic Press, 2001. ISBN: 9780123695161.

[15] Schuster, K., Unger, S., Aichele, C., Lindner, F., Grimm, S., Litzkendorf, D., Kobelke, J., Bierlich, J., Wondraczek, K. and Bartelt, H. *Advanced Optical Technologies* 3.4 (2014), pp. 447–468. DOI: doi:10.1515/aot-2014-0010. URL: https://doi.org/10.1515/aot-2014-0010.

[16] Sylvestre, T., Genier, E., Ghosh, A. N., Bowen, P., Genty, G., Troles, J., Mussot, A., Peacock, A. C., Klimczak, M., Heidt, A. M., Travers, J. C., Bang, O. and Dudley, J. M. Recent advances in supercontinuum generation in specialty optical fibers. *J. Opt. Soc. Am. B* 38.12 (Dec. 2021), F90–F103. DOI: 10.1364/JOSAB.439330. URL: https://opg.optica.org/josab/abstract.cfm?URI=josab-38-12-F90.

[17] Leal-Junior, A. G., Diaz, C. A., Avellar, L. M., Pontes, M. J., Marques, C. and Frizera, A. Polymer Optical Fiber Sensors in Healthcare Applications: A Comprehensive Review. *Sensors* 19.14 (2019). ISSN: 1424-8220. DOI: 10.3390/s19143156. URL: https://www.mdpi.com/1424-8220/19/14/3156.

[18] Snyder, A. W. *Optical waveguide theory*. eng. London: Chapman and Hall, 1983. ISBN: 0-412-09950-0.

[19] Polyanskiy, M. N. *Refractive index database*. https://refractiveindex.info/?shelf=main&book=SiO2&page=Malitson. Accessed on 2022-08-07.

[20] Boyd, R. W. *Nonlinear Optics*. eng. Academic Press, 2013. ISBN: 9780121216801.

[21] Siegman, A. E. *Lasers*. eng. Mill Valley, Calif: University Science Books, 1986. ISBN: 1-68015-237-8.

[22] Chong, A., Buckley, J., Renninger, W. and Wise, F. All-normal-dispersion femtosecond fiber laser. eng. *Optics express* 14.21 (2006), pp. 10095–10100. ISSN: 1094-4087.

[23] Renninger, W. H., Chong, A. and Wise, F. W. Area theorem and energy quantization for dissipative optical solitons. eng. *Journal of the Optical Society of America. B, Optical physics* 27.10 (2010), pp. 1978–1982. ISSN: 0740-3224.

[24] Chong, A., Renninger, W. H. and Wise, F. W. Environmentally stable all-normal-dispersion femtosecond fiber laser. eng. *Optics letters* 33.10 (2008), pp. 1071–1073. ISSN: 0146-9592.

[25] Lecourt, J.-B., Duterte, C., Narbonneau, F., Kinet, D., Hernandez, Y. and Giannone, D. All-normal dispersion, all-fibered PM laser mode-locked by SESAM. eng. *Optics express* 20.11 (2012), pp. 11918–11923. ISSN: 1094-4087.

[26] Aguergaray, C., Broderick, N. G. R., Erkintalo, M., Chen, J. S. Y. and Kruglov, V. Mode-locked femtosecond all-normal all-PM Yb-doped fiber laser using a nonlinear amplifying loop mirror. eng. *Optics express* 20.10 (2012), pp. 10545–10551. ISSN: 1094-4087.

[27] Svelto, O. *Principles of Lasers*. eng. 5th ed. 2010. New York, NY: Springer US, 2010. ISBN: 1-280-38174-4.

[28] Keller, U. and Tropper, A. C. Passively modelocked surface-emitting semiconductor lasers. eng. *Physics reports* 429.2 (2006), pp. 67–120. ISSN: 0370-1573.

[29] Ouyang, C., Shum, P., Wu, K., Wong, J. H., Lam, H. Q. and Aditya, S. Bidirectional passively mode-locked soliton fiber laser with a four-port circulator. eng. *Optics letters* 36.11 (2011), pp. 2089–2091. ISSN: 0146-9592.

[30] Chen, J., Zhao, X., Yao, Z., Li, T., Li, Q., Xie, S., Liu, J. and Zheng, Z. Dual-comb spectroscopy of methane based on a free-running Erbium-doped fiber laser. eng. *Optics express* 27.8 (2019), pp. 11406–11412. ISSN: 1094-4087.

[31] Saito, S., Yamanaka, M., Sakakibara, Y., Omoda, E., Kataura, H. and Nishizawa, N. All-polarization-maintaining Er-doped dual comb fiber laser using single-wall carbon nanotubes. eng. *Optics express* 27.13 (2019), pp. 17868–17875. ISSN: 1094-4087.

[32] Paschotta, R. *Ring resonators*. 2019. URL: https://www.rp-photonics.com/ring_resonators.html (visited on 07/15/2022).

[33] Ter-Mikirtychev, V. V. *Fundamentals of Fiber Lasers and Fiber Amplifiers*. eng. Vol. 181. Springer Series in Optical Sciences. Cham: Springer International Publishing AG, 2019. ISBN: 3030338894.

[34] Bale, B. G., Okhitnikov, O. G. and Turitsyn, S. K. Modeling and Technologies of Ultrafast Fiber Lasers. *Fiber Lasers*. John Wiley Sons, Ltd, 2012. Chap. 5, pp. 135–175. ISBN: 9783527648641. DOI: https://doi.org/10.1002/9783527648641.ch5. eprint: https://onlinelibrary.wiley.com/doi/pdf/10.1002/9783527648641.ch5. URL: https://onlinelibrary.wiley.com/doi/abs/10.1002/9783527648641.ch5.

[35] Rissanen, J. *PyFiberAmp documentation*. URL: https://www.pyfiberamp.com/.

[36] Giles, C. and Desurvire, E. Modeling erbium-doped fiber amplifiers. eng. *Journal of lightwave technology* 9.2 (1991), pp. 271–283. ISSN: 0733-8724.

[37] Haiml, M., Grange, R. and Keller, U. Optical characterization of semiconductor saturable absorbers. eng. *Applied physics. B, Lasers and optics* 79.3 (2004), pp. 331–339. ISSN: 0946-2171.

[38] Schreiber, T., Ortaç, B., Limpert, J. and Tünnermann, A. On the study of pulse evolution in ultra-short pulse mode-locked fiber lasers by numerical simulations. eng. *Optics express* 15.13 (2007), pp. 8252–8262. ISSN: 1094-4087.

[39] Lee, J., Kwon, S., Zhao, L. and Lee, J. H. Investigation into the impact of the recovery time of a saturable absorber for stable dissipative soliton generation in Yb-doped fiber lasers. eng. *Optics express* 29.14 (2021), pp. 21978–21991. ISSN: 1094-4087.